THE JOURNAL OF PHYSICAL CHEMISTRY A

Article

pubs.acs.org/JPCA

Elucidating the Decomposition Mechanism of Energetic Materials with Geminal Dinitro Groups Using 2-Bromo-2-nitropropane Photodissociation

Ryan S. Booth, Chow-Shing Lam, Matthew D. Brynteson, Lei Wang, and Laurie J. Butler*

The James Franck Institute and Department of Chemistry, The University of Chicago, Chicago, Illinois 60637, United States

Supporting Information

ABSTRACT: These experiments photolytically generate two key intermediates in the decomposition mechanisms of energetic materials with nitro substituents, 2-nitropropene, and 2-nitro-2-propyl radicals. These intermediates are produced at high internal energies and access a number of competing unimolecular dissociation channels investigated herein. We use a combination of crossed laser-molecular beam scattering and velocity map imaging to study the photodissociation of 2-bromo-2-nitropropane at 193 nm and the subsequent unimolecular dissociation of the intermediates above. Our results demonstrate that 2-bromo-2-nitropropane has four primary photodissociation pathways: C−Br bond fission yielding the 2-nitro-2-propyl radical, HBr elimination yielding 2-nitropropene, C−N bond fission yielding the 2-bromo-2-propyl radical, and HONO elimination yielding 2-bromopropene. The photofragments are formed with significant internal energy and undergo many secondary dissociation events, including the exothermic dissociation of 2-nitro-2-propyl radicals to NO + acetone. Calculations at the G4//B3LYP/6-311++g(3df,2p) level show that the presence of a radical at a nitroalkyl center changes the mechanism for and substantially lowers the barrier to NO loss. This mechanism involves an intermediate with a three-center ring rather than the intermediate formed during the traditional nitro−nitrite isomerization. The observed dissociation pathways of the 2-nitro-2-propyl radical and 2-nitropropene help elucidate the decomposition mechanism of larger energetic materials with geminal dinitro groups.

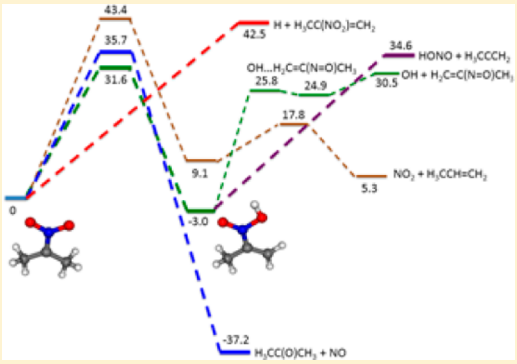

INTRODUCTION

The decomposition mechanisms of energetic materials have been studied both experimentally and theoretically for decades.[1−9] Despite this, the initial decomposition steps in materials such as TNAZ (1,3,3-trinitroazetidine) are still debated. In energetic materials containing NO_2 functional groups, there are three major initial steps: direct fission of either C−NO_2 or N−NO_2 bonds, concerted HONO elimination, or a nitro−nitrite isomerization yielding NO.[1] Interestingly, Bernstein and co-workers[2−5] have demonstrated that the initial step for dissociation of a large series of energetic materials (RDX, PETN, HMX, and CL-20) is dependent upon the method of excitation. For instance, after thermal excitation, ground state energy calculations for PETN (pentaerythritol tetranitrate) done at the ONIOM[CASSCF(6,6)/6-31G(d):UFF] level of theory suggest that a direct NO_2 loss channel is expected to dominate, as its barrier is only 0.97 eV compared to the 2.6 eV needed to undergo a nitro−nitrite isomerization.[5] However, if PETN is excited via a UV photon, a conical intersection between the ground and electronic state exists near the nitrite isomer making this isomerization the dominant step, as opposed to direct NO_2 loss.[5] Garland et al.[6] also showed that initial loss of NO dominates over the NO_2 loss pathway in TNAZ following UV irradiation.

This study, using two model systems, focuses on elucidating the subsequent dissociation steps following the C−NO_2 fission in energetic materials like TNAZ. Thus, we focus not on the first decomposition step in the mechanism, but on the subsequent steps after the initial loss of one of the NO_2 groups. Several of these materials share similar functionality, such as two NO_2 groups attached to the same atom (e.g., TNAZ and FOX-7) and strained rings (e.g., TNAZ and CL-20). After C−NO_2 fission, the resulting radical can undergo dissociation events such as loss of a second NO_2 group or a ring-opening reaction. Computational work on TNAZ at the B3LYP/6-31G(d,p) level by Alavi et al.[7] has shown that the ring-opening (with the simultaneous C═C π-bond formation) has a lower barrier (25 kcal/mol) than any of the other dissociation pathways (i.e., loss of a second NO_2). Therefore, this pathway is expected to be the major pathway following initial loss of NO_2. After the ring opens, there are several bond fission reactions available. Using infrared multiphoton dissoci-

Special Issue: Oka Festschrift: Celebrating 45 Years of Astrochemistry

Received: December 12, 2012
Revised: February 21, 2013

 © XXXX American Chemical Society

ation, Anex et al.[8] concluded that loss of a second NO_2 group is the preferred pathway. In contrast, Zhang and Bauer[1] induced thermal decomposition using shock-tubes and concluded that the molecule would undergo either C−N (on the nitro-alkyl chain) or C−C bond fission rather than lose another NO_2 group.

Instead of studying the decomposition of TNAZ directly, we study the unimolecular dissociation events of key intermediates similar to those along the path of TNAZ decomposition. By creating vibrationally excited mimetic molecules under collision-free conditions, we are able to isolate the secondary dissociation events more clearly than in bulk studies. The 2-nitro-2-propyl radical ($CH_3C(NO_2)CH_3$) is used as a mimic for TNAZ after the thermal fission of the first NO_2 but prior to ring-opening. This radical possesses the same secondary alkyl radical center and NO_2 moieties as TNAZ following loss of NO_2 (but lacks a strained ring). To study the resulting molecule after ring-opening, we use 2-nitropropene ($CH_3C(NO_2)=CH_2$), which mimics the nitropropene moiety in the TNAZ dissociation mechanism. Both of these mimetic molecules are created in situ by photodissociating 2-bromo-2-nitropropane with 193 nm light.

The C−Br photofission and OH loss channels of 2-bromo-2-nitropropane have been studied by Saha et al.[9] focusing on the mechanism for OH production; they used laser-induced fluorescence to detect the OH radicals produced by photolysis of 2-bromo-2-nitropropane at 193 nm light. Because of the limited detection scheme, they had difficulty investigating alternative primary photodissociation channels (aside from C−Br and C−NO_2 fission).

■ EXPERIMENTAL SECTION

Scattering Apparatus. A crossed laser−molecular beam scattering apparatus was used to take the majority of the data presented in this study. A beam of 2-bromo-2-nitropropane (97% from Sigma-Aldrich, used without further purification) is created by seeding the equilibrium vapor pressure of the liquid sample in helium to a total pressure of 400 Torr. This gaseous mixture is supersonically expanded through a continuous (not pulsed) nozzle with an orifice diameter of 0.15 mm that is heated to 150 °C. The expanded beam passes through two skimmers into the main chamber where it is intersected by unpolarized 193 nm photons from a Lumonics PM-848 excimer laser. The laser enters the chamber in a direction perpendicular to that of the molecular beam and the detector axis: it was focused to a ∼6 mm^2 spot with pulse energies of ∼2−3 mJ at the interaction region. The molecular beam is introduced to the main chamber by means of a rotatable source region. Following the photodissociation, the photofragments that have a net velocity vector (the vector sum of the molecular beam velocity and the velocity imparted during the primary photodissociation and the subsequent dissociation events) within the 1.5 degree acceptance angle of the detector enter the detector region. After traveling 45 cm from the intersection with the laser to the detector's ionization region, the fragments are ionized via 200 eV electron bombardment.[10] The ions are accelerated by a series of ion plates, mass selected by a quadrupole mass spectrometer, and then detected via a Daly detector.[11] The signal is binned with respect to the total flight time (neutral + ion) in 2 microsecond increments, and the counts for each bin were recorded using a multichannel scalar. All time-of-flight (TOF) spectra presented herein represent the neutral TOF, where the ion flight time has been subtracted out using the ion flight constant for the apparatus of 4.5 μs $amu^{-1/2}$. The speed distribution of the molecular beam is characterized by sending the beam directly on axis with the detector through a chopper wheel spinning at 300 Hz. A typical peak molecular beam speed in the number density distribution, $N(v)$, is 1690 m/s with a spread ($\Delta v/v_{peak}$) of 11% calculated from the full width at half-maximum (FWHM) of $N(v)$. The observed TOF spectra were fit via forward convolution using the CMLAB2 program.[12]

Velocity Map Imaging Apparatus. A velocity map imaging apparatus was used to collect supplemental data in this experiment. The apparatus is described in detail elsewhere, and only a brief description will be given here.[13−15] A beam of 2-bromo-2-nitropropane (97% from Sigma-Aldrich, used without further purification) is created by seeding the equilibrium vapor pressure of the liquid sample with helium to a total pressure of 500 Torr. The beam is supersonically expanded through a pulsed valve heated to 150 °C and passed through a skimmer, which collimates the beam. The molecules are then photodissociated using vertically polarized 193 nm light from a GAM excimer laser. This laser is focused to a ∼1 mm^2 spot, and the pulse energies are typically ∼0.5 mJ. Approximately 40 ns after photodissociation, the molecules are ionized by 118 nm light (10.5 eV photons) generated by tripling the 355 nm output of pulsed Nd:YAG laser in a xenon gas cell.[16]

The ions pass through an electrostatic lens assembly, which includes a repeller plate and an extractor plate held in a voltage ratio of 1.4:1. The lens assembly accelerates the ions down the grounded time-of-flight (TOF) tube toward the detector. The detector consists of a position sensitive Chevron microchannel plate (MCP) that is gated by applying a −750 V pulse that coincides with the arrival time of the mass of interest. The ion colliding with the MCP creates an electron cascade, which induces fluorescence on a phosphor screen directly behind the MCP. A CCD camera records the resulting images of the phosphor screen.

The speed distribution and angular distribution measured on the imaging apparatus were analyzed using the BASEX code of Dribinski et al.[17] When the detected speeds result from a primary photodissociation channel followed by subsequent dissociation of highly vibrationally excited radical or molecule product, we additionally use the code in Alligood et al.[18] This code accounts for the fact that the net velocity of the fragments detected in the image is the vector sum of the primary photodissociation recoil velocity and the additional velocity imparted in the secondary dissociation.

For select imaging spectra in this work, we photoionize the fragments with tunable VUV light generated by a resonance enhanced four-wave difference-frequency mixing ($\omega_{VUV} = 2\omega_1 - \omega_2$) scheme in a Kr gas cell (10−15 Torr), where ω_1 and ω_2 represent the fixed ultraviolet (UV) and tunable visible laser frequencies. The UV and visible laser light pulses are respectively generated by two dye lasers (Lambda Physik, FL3002), which are pumped by a common injection-seeded Nd:YAG laser (Continuum Powerlite Precision 9020). The fixed UV frequency ω_1 at 47046.43 cm^{-1} (212.56 nm) is obtained by the third harmonic generation of the laser output at 15682.14 cm^{-1} (637.67 nm) to match the two-photon resonance of the Kr transition, 5p ← 4p at 94 092.86 cm^{-1} ($2\omega_1$). The visible frequency ω_2 is generated by the second dye laser, which is tunable to give the desired VUV wavelengths. The resultant ω_{VUV} utilized as the photoionization source is selected by an off-center MgF_2 lens before entering the photoionization region.

Computational Methods. All energies are zero-point corrected (ZPE) and calculated at the G4//B3LYP/6-311++g(3df,2p) level[19] using the Gaussian 09 software package.[20]

RESULTS AND ANALYSIS

1. Photodissociation Channels of 2-Bromo-2-nitropropane, $CH_3C(NO_2)(Br)CH_3$. *A. Overview.* Our experimental results below give evidence of four primary photodissociation channels (eqs 1−4). The calculated endoergicities are shown with their associated channel.

$$CH_3C(NO_2)(Br)CH_3 + h\nu \rightarrow CH_3C(Br)CH_3 + NO_2 \quad \Delta H_{0K} = 54.0 \text{ kcal/mol} \tag{1}$$

$$CH_3C(NO_2)(Br)CH_3 + h\nu \rightarrow CH_3C(Br)CH_2 + HONO \quad \Delta H_{0K} = 15.7 \text{ kcal/mol} \tag{2}$$

$$CH_3C(NO_2)(Br)CH_3 + h\nu \rightarrow CH_3C(NO_2)CH_3 + Br \quad \Delta H_{0K} = 59.2 \text{ kcal/mol} \tag{3}$$

$$CH_3C(NO_2)(Br)CH_3 + h\nu \rightarrow CH_3C(NO_2)CH_2 + HBr \quad \Delta H_{0K} = 15.5 \text{ kcal/mol} \tag{4}$$

We use the word primary to mean the first processes resulting from photoexcitation at 193 nm, to distinguish them from the subsequent unimolecular dissociation of some of the vibrationally excited photoproducts, denoted as the secondary processes. The secondary processes are covered in later sections of this report, as they are the processes relevant to our investigation of radical and molecular intermediates in the thermal decomposition of energetic materials.

B. Primary C−NO_2 Photofission Yielding NO_2 and $CH_3C(Br)CH_3$. The velocity mapped images taken at m/e = 123 ($CH_3C(^{81}Br)CH_3^+$) and m/e = 121 ($CH_3C(^{79}Br)CH_3^+$) in the proper isotope ratio evidence primary C−NO_2 photofission (eq 1). The speed distribution, $P(v)$, derived from the m/e = 123 image is presented in Figure 1, and the corresponding recoil kinetic energy distribution (hereafter, $P(E_T)$) for C−NO_2 photofission is shown as red dots in Figure 2. Since the NO_2 is momentum matched to its $CH_3C(Br)CH_3$ cofragment, forward convolution fitting using the red $P(E_T)$ in Figure 2 should fit

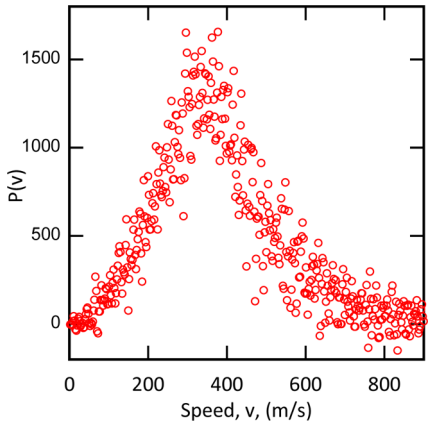

Figure 1. Speed distribution derived from the m/e = 123 ($CH_3C(^{81}Br)CH_3^+$) image. Data are shown in red circles. It is assigned to the cofragment formed in C−NO_2 photofission (eq 1).

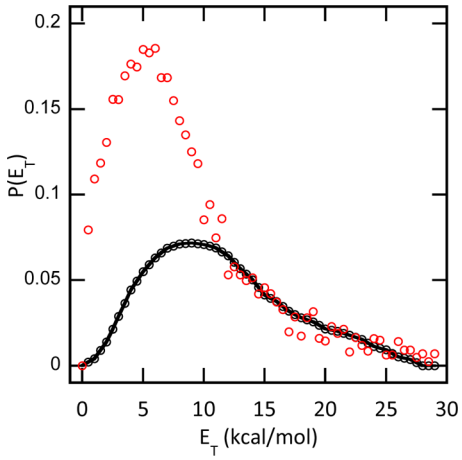

Figure 2. Photofragment recoil kinetic energy distribution for C−NO_2 fission (eq 1) in 2-bromo-2-nitropropane at 193 nm. The total $P(E_T)$ shown in red circles is derived from the imaging speed distribution of the cofragment shown in red circles in Figure 1. The partial $P(E_T)$ shown in black circles was derived from forward convolution fitting of the signal arriving between 130 and 200 μs in the m/e = 46 (NO_2^+) TOF (Figure 3); this signal represents the NO_2 photofragments that were not lost to secondary photodissociation (Section 5.B).

the corresponding signal in the m/e = 46 (NO_2^+) TOF spectrum (Figure 3) taken in our scattering apparatus if neither

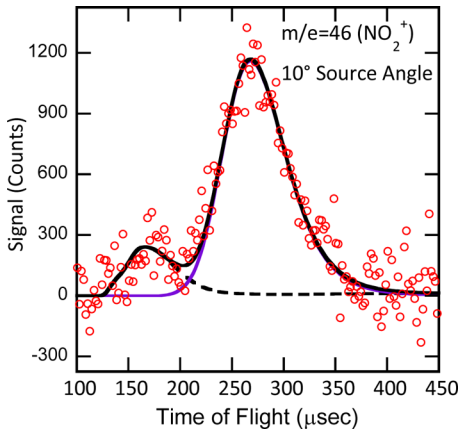

Figure 3. Time-of-flight spectrum taken at m/e = 46, NO_2^+. Data are shown in red circles. The remaining NO_2 product from C−NO_2 photofission (eq 1) is fitted as a dashed black line using the partial $P(E_T)$ shown in black circles in Figure 2. The contribution shown as a purple line is from the dissociation of molecular clusters in the beam. Adapted from ref 29. Copyright 2012 American Chemical Society.

is lost to subsequent dissociation processes. However, in early experiments on nitromethane photodissociation,[21] the fraction of the NO_2 product with lower recoil kinetic energies upon C−NO_2 fission at 193 nm were lost to secondary photodissociation, as they efficiently absorbed a second 193 nm photon. We expect a similar issue in these experiments, so we fit the measured m/e = 46 TOF spectrum to derive the $P(E_T)$ of the NO_2 photofragments that did not undergo secondary photodissociation. The forward convolution fit shown in the dashed black line in the m/e = 46 TOF (Figure 3) gives the $P(E_T)$ shown in black dots in Figure 2. This remaining NO_2 $P(E_T)$ derived from the m/e = 46 TOF signal is very similar to the high kinetic energy portion of the total C−NO_2

photofission $P(E_T)$, derived from fitting the m/e = 123 ($CH_3C(^{81}Br)CH_3^+$) data, but shows that a large portion of the NO_2 photofragments formed with lower recoil kinetic energies were lost to a subsequent photodissociation process. Later in this report, we fit the NO products from the NO_2 fragments that undergo $NO_2 + h\nu \rightarrow NO + O$. Both $P(E_T)$s in Figure 2, the total C−NO_2 photofission $P(E_T)$ derived from the m/e = 123 $P(v)$ and the one derived from signal in the m/e = 46 TOF from NO_2 that did not absorb an additional photon, are strikingly similar to those observed for the photodissociation of nitromethane at 193 nm.[21] In the nitromethane study, the multiphoton absorption was confirmed by a laser power dependence of the contributions to the m/e = 30 TOF spectrum. In nitromethane, the momentum matched alkyl fragment, CH_3, does not have enough vibrational energy to undergo secondary unimolecular dissociation, while our cofragment, $CH_3C(Br)CH_3$, can and does. However, the probability of this secondary dissociation in our system is not strongly correlated to the energy partitioned to translation in the primary C−NO_2 photofission. This is not surprising as the range of recoil kinetic energies is relatively small compared to the available energy and is distributed between the NO_2 and $CH_3C(Br)CH_3$ photofragments.

C. Primary HONO Elimination Yielding HONO and $CH_3C(Br)=CH_2$. The velocity map images at m/e = 122 ($CH_3C(^{81}Br)=CH_2^+$) and m/e = 120 ($CH_3C(^{79}Br)=CH_2^+$), in the proper isotope ratio, evidence HONO photoelimination (eq 2). The signal cannot be attributed to dissociative ionization of $CH_3C(Br)CH_3$ (mass 123) since the appearance energy is calculated at 11.23 eV, which is inaccessible at our photoionization energy of 10.5 eV. The speed distribution derived from the m/e = 122 ($CH_3C(^{81}Br)=CH_2^+$) image is shown in Figure 4. This imaging speed distribution includes a signal from this primary channel (blue circles) and the contribution from a secondary dissociation channel discussed in Section 5.C. The total signal is shown in red circles. The $P(E_T)$ for primary HONO elimination is obtained from the blue circles in Figure 4 and shown in Figure 5. Although no signal appears at m/e = 47 ($HONO^+$), HONO is known to undergo dissociative ionization to both m/e = 30 (NO^+) and m/e = 17 (OH^+) upon electron bombardment ionization. However, in this case, the HONO photofragment is assumed to have enough energy to surmount the relatively low calculated reaction barrier energy of 49.9 kcal/mol to neutral NO + OH (see Section 4.B)

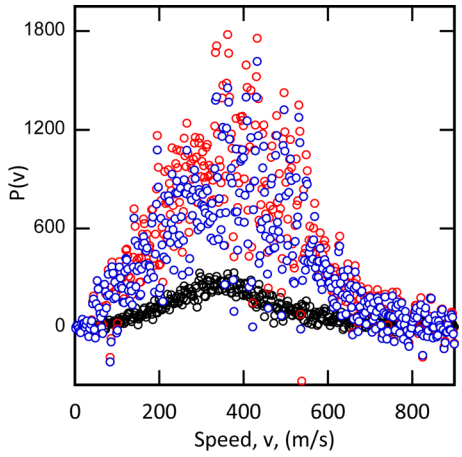

Figure 4. Speed distribution derived from the m/e = 122 ($CH_3C(^{81}Br)=CH_2^+$) image. Data are shown as red circles. The contribution from the cofragment formed in HONO photoelimination (eq 2) is shown in blue. It was obtained by subtracting the imaging speed distribution shown in black representing the contribution of $CH_3C(Br)=CH_2$ fragments resulting from secondary H-loss from vibrationally excited $CH_3C(Br)CH_3$ radicals formed after primary NO_2 loss from 2-bromo-2-nitropropane (eq 1) because the two contributions overlap so strongly. The scaling of the black circles is relatively arbitrary, so the product branching may not be extracted from the data.

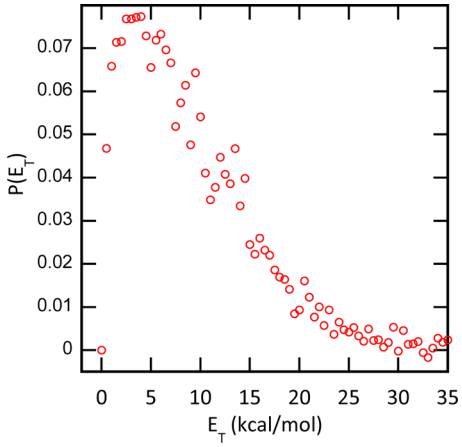

Figure 5. Photofragment recoil kinetic energy distribution for HONO photoelimination (eq 2) in 2-bromo-2-nitropropane at 193 nm. The total $P(E_T)$ is derived from the imaging speed distribution of the cofragment shown in blue in Figure 4. Some uncertainty results from the subtraction of the overlapping signal shown in black in Figure 4.

D. Primary C−Br Bond Photofission Yielding Br and $CH_3C(NO_2)CH_3$. The C−Br photofission primary channel (eq 3) is evidenced by the sharp peak in the m/e = 79 (Br^+) TOF spectra taken on the scattering apparatus and shown in Figure 6 at three different source angles. Although there are other contributions to the m/e = 79 (Br^+) TOF spectra arising from dissociative ionization of other products, which will be discussed in later sections, the fast sharp peak is characteristic of C−Br photofission via a repulsive excited state. The 193 nm photodissociation of alkyl bromides in general result in similar C−Br photofission channels. A forward convolution fit using the $P(E_T)$ in Figure 7 gives the purple line fit in the m/e = 79 (Br^+) TOF spectra at three source angles in Figure 6.

We determine the internal energy of the $CH_3C(NO_2)CH_3$ fragment by invoking conservation of energy. Thus, after photofission, the remaining energy must be partitioned into the rotational and vibrational energy of the radical. The fairly low dissociation energy for the C−Br bond (59.2 kcal/mol) yields a vibrational energy distribution for the $CH_3C(NO_2)CH_3$ radicals, the entirety of which is above the lowest barrier to further dissociation. The partitioning of energy into rotation is expected to be small, thus all of the $CH_3C(NO_2)CH_3$ radicals possess high vibrational energy and will undergo secondary dissociation. The relatively low C−Br bond energy is attributed to delocalization of the radical via the NO_2 group. This is one of the two key intermediates examined in this work.

E. HBr Elimination Yielding HBr and $CH_3C(NO_2)=CH_2$. The final primary photodissociation channel is the elimination of HBr (eq 4), which gives signal at m/e = 80 ($H^{79}Br^+$). A forward convolution fit using the $P(E_T)$ shown in Figure 8 gives

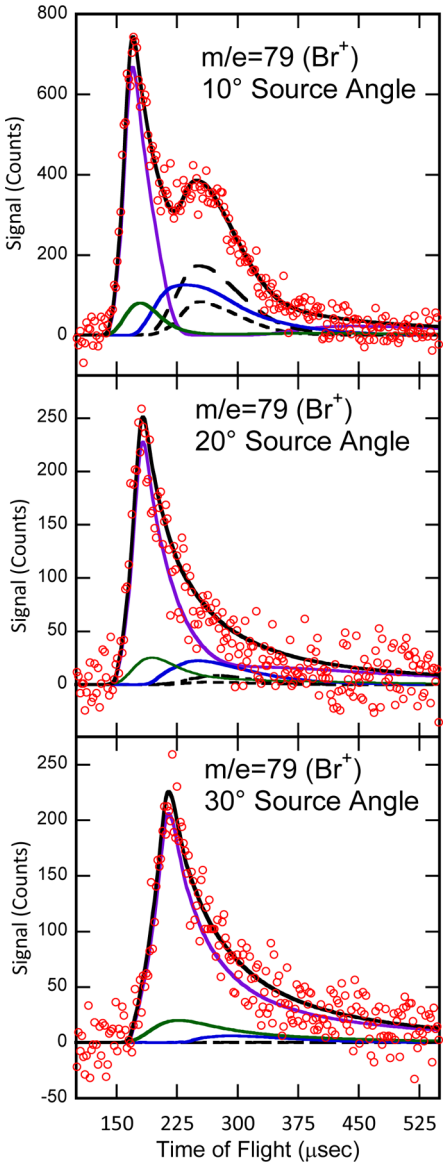

Figure 6. Time-of-flight spectrum taken at m/e = 79, Br^+. Data are shown as red circles. The Br atom products from C−Br photofission (eq 3), shown by the purple fit, are used to derive the C−Br photofission $P(E_T)$ shown in Figure 7. Dissociative ionization from HBr products arising from primary HBr photoelimination is shown as the blue fit. Dissociative ionization of the HBr fragments arising from secondary HBr loss from vibrationally excited $CH_3C(Br){=}CH_2$ species (Section 5.C) is shown as the green fit. Dissociative ionization of the $CH_3C(Br){=}CH_2$ (cofragment to primary HONO elimination) and $CH_3C(Br)CH_3$ (cofragment of primary C−N bond fission) are shown by the long dashed and short dashed black fits, respectively. Note that the bottom frame (30° source angle) was taken at a nozzle temperature of 88 °C.

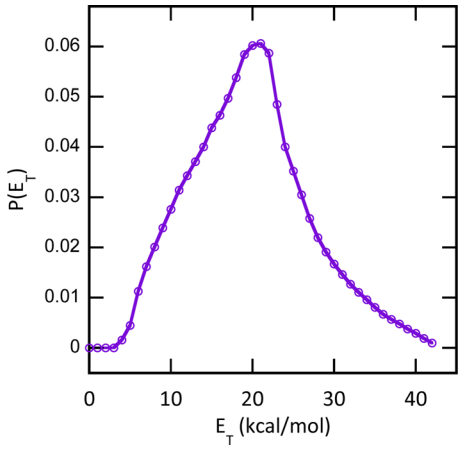

Figure 7. Photofragment recoil kinetic energy distribution for C−Br fission (eq 3) in 2-bromo-2-nitropropane at 193 nm. The $P(E_T)$ is derived from the forward convolution fit of the signal shown by the purple line in Figure 6 representing signal from the Br atom primary photoproduct.

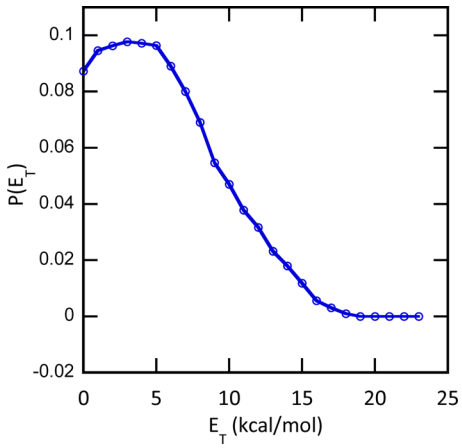

Figure 8. Photofragment recoil kinetic energy distribution for HBr photoelimination (eq 4) in 2-bromo-2-nitropropane at 193 nm. The $P(E_T)$ is derived from the forward convolution fit shown as a blue line in the time-of-flight spectrum taken at m/e = 80 (HBr^+) shown in Figure 9, the signal assigned to the HBr primary photoproduct.

the blue line fit in the m/e = 80 ($H^{79}Br^+$) TOF spectrum shown in Figure 9. The fast portion of the signal not fit by this $P(E_T)$ is attributed to a secondary channel originating from primary HONO elimination. Because of the low endoergicity of this channel it is likely a large amount of vibrational energy will be partitioned into the HBr and $CH_3C(NO_2){=}CH_2$ fragments, and therefore, it is expected that most of the $CH_3C(NO_2){=}CH_2$ will undergo secondary dissociation events. The slowest portion of the m/e = 80 (HBr) TOF is attributed to the dissociative ionization of stable $CH_3C(Br)CH_3$ (Section 1.B) and $CH_3C(Br){=}CH_2$ (Section 1.C)

F. Branching Ratio between C−Br Fission and HBr Elimination. The branching ratio between C−Br photofission (eq 3) and HBr photoelimination (eq 4) may be calculated via eq 5.

$$\frac{\Phi_{Br}}{\Phi_{HBr}} = \left(\frac{R_{prob}(C{-}Br)}{R_{prob}(HBr)}\right)\left(\frac{\sigma_{tot,HBr}}{\sigma_{tot,Br}}\right)\left(\frac{f(Br^+/HBr)}{f(Br^+/Br)}\right) \quad (5)$$

The branching ratio is calculated from the relative amount of signal from each process observed in the m/e = 79 (Br^+) TOF spectra. The R_{prob} values in eq 5 are data fitting parameters we determine by fitting the observed signal from a particular channel while assuming that all of the electron bombardment cross sections are equivalent. They include the usual correction for kinematic factors such as the Jacobian factors inherent in the signal in the TOF spectra and the different sensitivity to each product due to transit time in the electron bombardment ionizer. The R_{prob} values have some uncertainty in this case

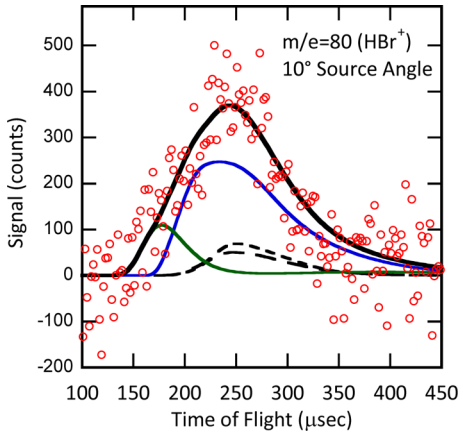

Figure 9. Time-of-flight spectrum taken at m/e = 80, HBr^+. Data are shown as red circles. The HBr products from HBr photoelimination (eq 4) is fit by the blue line and is used to derive the HBr photoelimination $P(E_T)$ shown in Figure 8. The HBr fragments arising from secondary HBr loss from vibrationally excited $CH_3C(Br){=}CH_2$ species (Section 4.C) are shown as the green fit. The HBr fragments arising from dissociative ionization of stable $CH_3C(Br){=}CH_2$ and $CH_3C(Br)CH_3$ fragments are shown as the black long dashed and short dashed line fits, respectively.

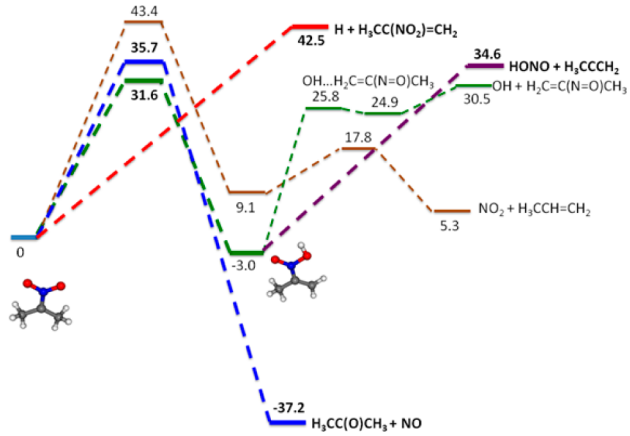

Figure 10. Calculated minima and transition states for the possible dissociation channels of the 2-nitro-2-propyl radical ($CH_3C(NO_2)$-CH_3) on the ground state potential energy surface. All energies are expressed in units of kcal/mol and were calculated at the G4//B3LYP/6-311++g(3df,2p) level. The experimentally observed pathways are shown with thicker lines and bolded text.

because there are other overlapping contributions in the m/e = 79 TOF; therefore, the contribution of each particular channel cannot be absolutely certain. The σ_{tot} value represents the total electron bombardment ionization cross-section for each species and is calculated for both HBr and Br in ref 22. The f value represents the fraction of cations at the detected mass. For example, the $f(Br^+/HBr)$ represents the fraction of ionized HBr, which appears at Br^+. This value is experimentally determined via mass spectroscopy and reported in ref 23 for HBr and experimentally determined for Br in ref 24 (A substantial fraction of Br atoms appear at Br^{2+}, so the total ionization cross-section from ref 22 of 3.56 Å^2 is adjusted by the factor of 3.2/3.9 because we are fitting the signal at Br^+ only).

$$\frac{\Phi_{Br}}{\Phi_{HBr}} = \left(\frac{0.843}{0.086}\right)\left(\frac{3.30\text{Å}^2}{3.56\text{Å}^2}\right)\left(\frac{\frac{39}{139}}{\frac{3.2}{3.9}}\right) = 3 \tag{6}$$

The term $f(Br^+/HBr)$ = 39/139 accounts for the fact that the published mass spectrum of HBr[23] is dominated by Br^+ and HBr^+, in a ratio of 39:100; so in using this, we assume that the vibrationally excited HBr formed photolytically would have the same mass spectrum. The experimental branching ratio of C−Br photofission/HBr photoelimination is thus determined to be 3:1. Although the partial ionization cross-sections used here are accurate to better than 10%, the two contributions to the m/e = 79 TOF spectra overlap other signals in the spectra, so the uncertainty in this branching ratio is substantial.

2. Dissociation of Vibrationally Excited $CH_3C(NO_2)CH_3$ Resulting from Primary C−Br Fission. *A. Overview.* The vibrationally excited $CH_3C(NO_2)CH_3$ radical formed from C−Br photofission could potentially undergo five secondary dissociation channels. We calculated the relevant stationary points for each channel shown in Figure 10. All energies are relative to the zero-point corrected G4 energy of 2-nitro-2-propyl radical. The pathway with the lowest barrier, 31.6 kcal/mol, begins with H atom transfer to the NO_2 group to form a radical with a HONO moiety ($CH_3C(NO_2)CH_3 \rightarrow CH_3C(NO_2H){=}CH_2$). Figure 10 shows two possible dissociation processes subsequent to this isomerization. One is a simple bond fission to yield HONO + CH_3CCH_2 with a barrier of 34.6 kcal/mol. The second path involves formation of a hydrogen-bonded complex between the OH and the lone pair of the N atom on the conjugated C=C−N=O moiety with a transition state energy of 25.8 kcal/mol; the actual complex is only slightly lower in energy, 24.9 kcal/mol. This complex can dissociate to give OH + $CH_3C(NO){=}CH_2$; the total endoergicity from the 2-nitro-2-propyl radical is 30.5 kcal/mol. The third possible decomposition channel for the vibrationally excited $CH_3C(NO_2)CH_3$ radical occurs over a barrier of 35.7 kcal/mol to give NO + $CH_3C(O)CH_3$ via an isomerization to a $CH_3C(O)(NO)CH_3$ intermediate followed by cleavage of the C−N bond. The $CH_3C(O)(NO)CH_3$ is not a true minimum and only exists en route to the NO + $CH_3C(O)CH_3$ dissociation. The difference between this isomerization and the traditional nitro−nitrite isomerization will be examined in the discussion section. The fourth channel is C−H bond fission (ΔH_{0K} = 42.5 kcal/mol) to give H + $CH_3C(NO_2){=}CH_2$. The fifth channel begins with a 1,2-hydrogen shift, with a barrier of 43.4 kcal/mol, followed by fission of the C−N bond to yield NO_2. The data below give evidence for three of the five secondary dissociation channels. These three pathways are designated by thicker lines and bolded text in Figure 10.

B. Dissociation of the $CH_3C(NO_2)CH_3$ Radical to OH + $CH_2C(N{=}O)CH_3$. Although the dissociation of vibrationally excited 2-nitro-2-propyl radicals to form OH + $CH_2C(N{=}O)CH_3$

$$CH_3C(NO_2)CH_3 \rightarrow CH_3C(NO_2H)CH_2 \rightarrow OH + CH_2C(N{=}O)CH_3 \tag{7}$$

has the lowest barrier of all of the secondary channels, we cannot definitively identify it in our data. The OH radical has a high ionization energy (13.0 eV) so we cannot detect it on our imaging apparatus, and with 200 eV electron impact ionization, many of the other primary and secondary products can dissociatively ionize to m/e = 17 (OH^+). This makes it difficult to use the OH^+ signal to diagnose individual channels.

There is also no definitive evidence for the $CH_2C(N{=}O)CH_3$ fragment. Sakaizumi et al.[25] demonstrated that $CH_2C(N{=}O)CH_3$ gives strong signal at m/e = 71 ($CH_2C(N{=}O)CH_3^+$) under 11.0 eV photoionization. In our experiment, however, there was no signal above background at m/e = 71 ($CH_2C(N{=}O)CH_3^+$) using both 10.5 eV photoionization and 200 eV electron bombardment ionization, although it is possible for $CH_2C(N{=}O)CH_3$ to dissociatively ionize to m/e = 41 ($CH_2CCH_3^+$) with an appearance energy (AE) of 9.7 eV. To determine whether this was occurring, we took velocity map images at m/e = 41 at 10.5 and 8.87 eV, and the two resulting speed distributions are compared in the lower frame of Figure 11. It is clear that the 8.87 eV spectrum has slightly decreased contribution from the fastest speeds (~1200−1700 m/s). The fragments arriving at these speeds could be attributed to the dissociative ionization of the $CH_2C(N{=}O)CH_3$ fragment. The contribution of this channel is difficult to ascertain accurately since the slow fragments in the m/e = 41 $P(v)$ are also from a dissociative ionization process, of $CH_3C(Br)CH_3$, with an AE of 9.2 eV (Section 5.E). Despite this ambiguity, it is clear that the extent of this channel is small since there is no signal above background at m/e = 71 even at 8.87 eV.

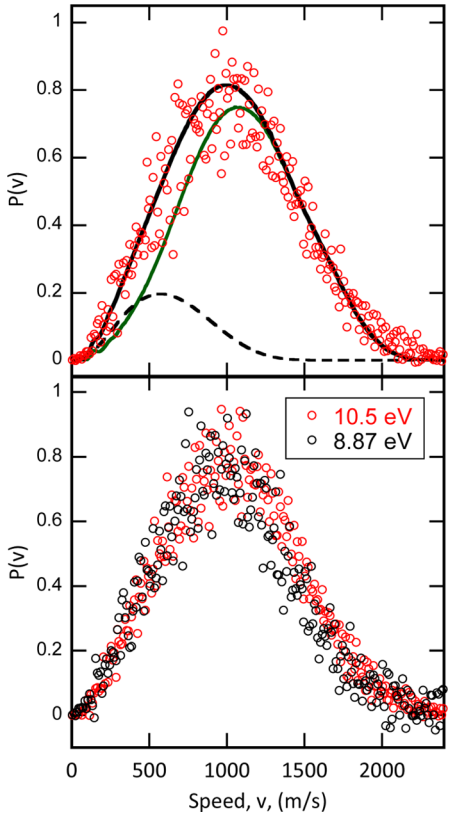

Figure 11. The upper frame shows the speed distribution derived from the m/e = 41 ($CH_3CCH_2^+$) image taken at 10.5 eV ionization energy. Data are shown as red circles. The green fit shows the contribution from CH_3CCH_2 products from the dissociation of 2-nitro-2-propyl radical to HONO + CH_3CCH_2 (eq 8); the fit is calculated using the $P(E_T, 2°)$ in Figure S4, Supporting Information. The short dashed black line contribution to the spectrum is from the dissociative ionization of stable $CH_3C(Br)CH_3$ radicals arising from primary C−NO_2 photofission. The lower frame compares the speed distributions derived from the m/e = 41 ($CH_3CCH_2^+$) image taken at ionization energies of 10.5 eV (red circles) and 8.87 eV (black circles).

Since this is a minor channel, the data presented hereafter is fit according to the assumption that the OH + $CH_2C(N{=}O)CH_3$ channel does not occur. For completeness, the $P(E_T)$ attributed to this channel is shown in the Supporting Information as Figure S1, as well as the predicted TOF and speed distribution for the OH cofragment in Figures S2 and S3, respectively, via forward convolution fitting. The OH fragment has arrival times around 100 μs and lies in the fastest portion of the m/e = 17 TOF. Interestingly, the predicted net speed of the OH fragments peaks at ~3000 m/s, which matches the speed observed by Saha et al.[9] of 2900 m/s.

C. Dissociation of the $CH_3C(NO_2)CH_3$ Radical to HONO + CH_3CCH_2. The dissociation of the 2-nitro-2-propyl radical to form HONO

$$CH_3C(NO_2)CH_3 \rightarrow CH_3C(NO_2H)CH_2 \rightarrow HONO + CH_3CCH_2 \quad (8)$$

begins with an H atom transfer to the NO_2 forming a HONO moiety. This isomer then undergoes C−N bond fission to give HONO (eq 8). The m/e = 41 TOF spectrum, shown in Figure 12, is bimodal, with the slow section consisting of other secondary dissociation channels and fragments arising from dissociative ionization. Although the m/e = 41 TOF has several contributions from dissociative ionization, the only fragment arising from these processes that possesses high enough recoil velocities to contribute to the fast peak is $CH_3CCH_2^+$ arising from the $CH_3C(NO_2)CH_2$ fragment formed in the H-loss channel described below in Section 2.E. The remainder of this fast peak is attributed to the CH_3CCH_2 fragment arising from the secondary dissociation of the 2-nitro-2-propyl radical to form HONO (eq 8).

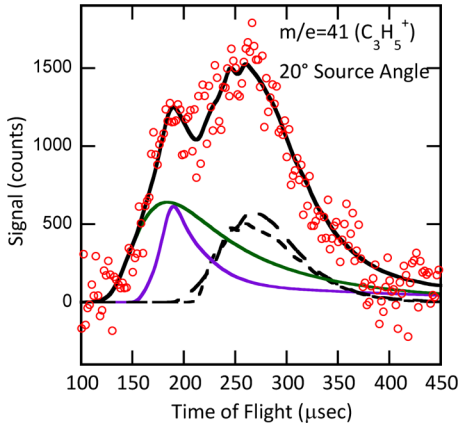

Figure 12. Time-of-flight spectrum taken at m/e = 41, $CH_3CCH_2^+$. Data are shown as red circles. The green fit shows the contribution from CH_3CCH_2 products from the dissociation of 2-nitro-2propyl radical to HONO + CH_3CCH_2 (eq 8); the fit is calculated using the $P(E_T, 2°)$ in Figure S4, Supporting Information. The signal peaking near 190 μs, fit in purple line, is assigned to the $CH_3C(NO_2){=}CH_2$ products from the dissociation of 2-nitro-2-propyl radicals to $CH_3C(NO_2){=}CH_2$ + H and is determined by the $P(E_T)$ in Figure 7 as the H atom is light compared to the $CH_3C(NO_2){=}CH_2$ fragment. The slowest signal (>230 μs) is assigned to dissociative ionization of stable $CH_3C(Br)CH_3$ radicals from primary NO_2 loss (short dashed black fit) and stable $CH_3C(Br){=}CH_2$ fragments from primary HONO elimination (long dashed black fit).

To confirm the dissociation of 2-nitro-2-propyl radical to HONO + CH_3CCH_2, we also detected the CH_3CCH_2 product in the velocity map imaging apparatus, as that spectrum would not include the signals from dissociative ionization that we observe with 200 eV electron bombardment detection. The speed distribution derived from the m/e = 41 image is shown in Figure 11. Upon 10.5 eV photoionization, there is no longer any contribution from dissociative ionization of the $CH_3C(NO_2)CH_2$ fragment product formed in the H-loss channel (Section 2.E), so the majority of the imaging speed distribution is fit by dissociation of 2-nitro-2-propyl radical to HONO + CH_3CCH_2. The only other channel capable of producing fragments with high enough velocity to contribute to the fast edge of Figure 11 is loss of NO_2 following HBr primary elimination, but there is no observed secondary NO_2 signal, so we discount this source of m/e = 41. The remaining signal, at speeds less than 1000 m/sec, is attributed to the dissociative ionization of the cophotofragment, $CH_3C(Br)CH_3$, formed in the C−NO_2 primary photofission channel (eq 1), as explained in the next paragraph.

The distribution of recoil kinetic energies imparted to the secondary fragments, $P(E_T, 2°)$, when the 2-nitro-2-propyl radicals dissociate to HONO + CH_3CCH_2 (eq 8) is given in Figure S4, Supporting Information. A forward convolution fit using this $P(E_T, 2°)$, building on the primary velocities of the dissociating radical from the C−Br photofission $P(E_T)$ in Figure 7, gives the green line fit in both the m/e = 41 TOF (Figure 12) and imaging speed distribution (Figure 11). The unfit part of the m/e = 41 imaging speed distribution in Figure 11 is too slow for any possible recoil velocity from this secondary channel and is therefore attributed to dissociative ionization of $CH_3C(Br)CH_3$ to $CH_3CCH_2^+$, where $CH_3C(Br)CH_3$ is from primary C−NO_2 photofission. Although no signal is seen for the cofragment HONO at m/e = 47 ($HONO^+$), HONO has been shown in previous work[26] to dissociatively ionize to both m/e = 17 (OH^+) and m/e = 30 (NO^+) under electron bombardment ionization. A forward convolution fit using the $P(E_T, 2°)$ in Figure S4, Supporting Information, is shown as a green line in the m/e = 30 TOF (Figure 13) and m/e = 17 TOF (Figure 14).

D. Dissociation of the $CH_3C(NO_2)CH_3$ Radical to $(CH_3)_2CO$ + NO. Formation of NO product from the secondary dissociation of vibrationally excited 2-nitro-2-propyl radical

$$CH_3C(NO_2)CH_3 \rightarrow CH_3C(O)(NO)CH_3 \rightarrow (CH_3)_2CO + NO \quad (9)$$

is extremely exothermic (−37 kcal/mol) giving the products significant internal and translational energy. This is apparent in the m/e = 30 (NO^+) TOF spectrum and imaging speed distribution (Figures 13 and 15, respectively), as both show a component of the NO signal with high recoil velocities. The speeds observed for the NO produced via eq 9 measured in the imaging apparatus, v_{net}(NO), are the vector sums of the velocity imparted to $CH_3C(NO_2)CH_3$ in the primary C−Br photofission and the additional velocity imparted to the secondary NO product when the $CH_3C(NO_2)CH_3$ dissociates to NO + acetone (eq 9). The net speed is measured to be as large as 4000 m/s. (Note that the imaging data in Figure 15 detects only the NO products from eq 9 since we use 10.5 eV photoionization, while the m/e = 30 TOF includes the NO^+ signal from the dissociative ionization of several polyatomic products). The black line fit shown in Figure 16 is a direct

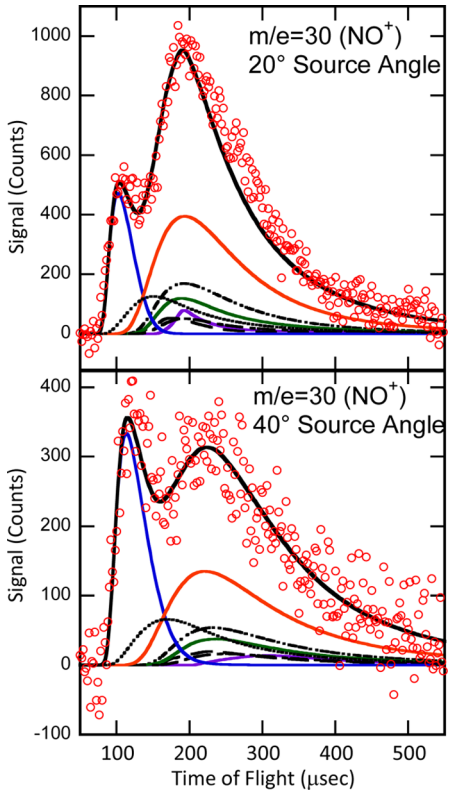

Figure 13. Time-of-flight spectrum taken at m/e = 30, NO^+ at source angles of 20° and 40° (upper and lower frames, respectively). Data are shown as red circles. The blue fit represents the contribution of NO fragments from the dissociation of $CH_3C(NO_2)CH_3$ to NO + $CH_3C(O)CH_3$ (eq 9) using the $P(E_T)$ in Figure 19. The dissociative ionization of HONO from the secondary dissociation of $CH_3C(NO_2)CH_3$ (eq 8), from primary C−Br fission, and $CH_3C(NO_2)CH_2$ (eq 12), from primary HBr elimination, are given by the solid green fit and the dash−dot black fit, respectively. The NO products from secondary dissociation of $CH_3C(NO_2)CH_2$ to NO + $CH_3C(O)CH_2$ (eq 15) are given by the double dash−dot black fit and use the $P(E_T)$ in Figure S7, Supporting Information. The orange fit shows the contribution of NO fragments arising from secondary dissociation of vibrationally hot HONO fragments from primary HONO elimination (eq 16) and uses the $P(E_T)$ shown in Figure S9, Supporting Information. The short dashed black fit shows the NO resulting from photodissociation of NO_2 products formed after primary NO_2 loss (eq 1) and uses the $P(E_T)$ shown in Figure S11, Supporting Information. The purple fit shows the dissociative ionization of $CH_3C(NO_2)CH_2$ fragments resulting from secondary H-loss from the $CH_3C(NO_2)CH_3$ radical (eq 10). The long dashed black fit shows the dissociative ionization of $CH_3C(Br)CH_3$ from primary C−NO_2 fission. Note that the lower frame (40° source angle) was taken at a nozzle temperature of 88 °C. Adapted from ref 29. Copyright 2012 American Chemical Society.

conversion of the m/e = 30 $P(v)$ (Figure 15) to a TOF and identifies the signal from neutral NO in the m/e = 30 TOF. The blue line fit in Figure 16 represents the sum of all neutral NO species from the fits in Figure 13; the similarity of the two lines in Figure 16 shows that the neutral NO product channels are weighted correctly in the m/e = 30 TOF.

This is the only secondary dissociation channel of the 2-nitro-2-propyl radical capable of imparting such high net speeds to the NO product. Therefore, most of the high velocity peak, at early arrival times in Figure 13 and at high net speeds in Figure 15, is attributed to this channel. Since the fast portion of

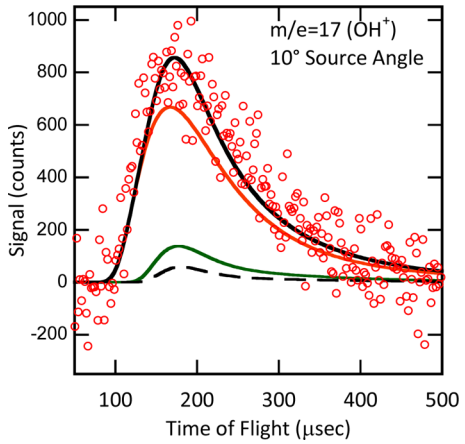

Figure 14. Time-of-flight spectrum taken at m/e = 17, OH^+. Data are shown as red circles. The orange fit shows the contribution of OH products from the dissociation of the vibrationally hot HONO photoelimination products of eq 2. The green fit and the dashed black fit are both from dissociative ionization of stable HONO formed from secondary dissociation events. The green fit shows a signal from HONO produced by vibrationally hot $CH_3C(NO_2)CH_3$ radicals (following primary C−Br photofission), and the black dashed line fit shows a signal from HONO arising from vibrationally excited $CH_3C(NO_2){=}CH_2$ fragments (following primary HBr elimination). The scaling of these fits is somewhat arbitrary as it is difficult to get quantitative branching ratios from this system.

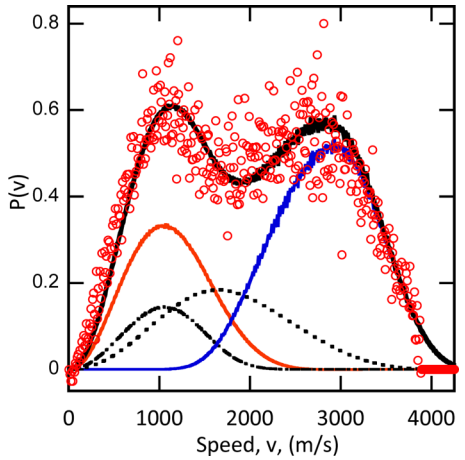

Figure 15. Speed distribution derived from the m/e = 30 (NO^+) image. Data are shown as red circles. The sharp drop just below 4000 m/s is from the products being scattered off the active area of the detector. The contribution from the NO product from the dissociation of 2-nitro-2-propyl radicals to NO + acetone (eq 9) is fit by the blue line using the $P(E_T, 2°)$ shown in Figure 19. The contribution of NO products from the dissociation of 2-nitropropene to NO + $CH_3C(O)CH_2$ (eq 13) is shown as the double dash−dot black fit; this fit uses the $P(E_T, 2°)$ in Figure S7, Supporting Information. The NO resulting from unimolecular dissociation of vibrationally hot HONO fragments formed upon primary HONO elimination is shown by the orange fit and uses the $P(E_T, 2°)$ in Figure S9, Supporting Information. The NO via secondary photodissociation of NO_2 products formed from primary C−NO_2 photofission is shown as the short dashed black line and uses the $P(E_T, 2°)$ in Figure S11, Supporting Information.

the m/e = 30 TOF includes signal from the high velocity NO products that are formed when a portion of the NO_2 photoproduct, from primary C−NO_2 photofission, absorbs a

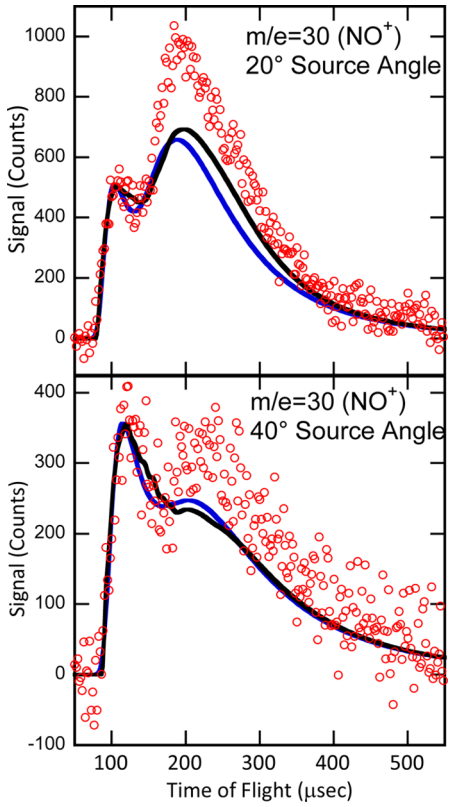

Figure 16. Time-of-flight spectrum taken at m/e = 30, NO^+, at source angles of 20° and 40° (upper and lower frames, respectively). Data are shown as red circles. The solid black fit is derived by direct conversion of the m/e = 30 $P(v)$ into a TOF spectrum. The solid blue line fit is the sum of signal from neutral NO products taken from Figure 13.

second 193 nm photon and dissociates to NO + O (see section 5.B), it is easier to assign signal from the NO + acetone channel via the cofragment $(CH_3)_2CO$. Although there was no signal detected at m/e = 58 ($(CH_3)_2CO^+$), the majority of $(CH_3)_2CO$ molecules will dissociatively ionize to m/e = 43 (CH_3CO^+) under electron bombardment. In addition, the only other channel capable of giving significant signal to the m/e = 43 TOF (Figure 17) is the CH_2NO + CH_3CO channel following primary HBr elimination (section 3.C) but there is no evidence for this channel. Therefore, the entirety of the m/e = 43 TOF (Figure 17) is assigned to the secondary dissociation of 2-nitro-2-propyl radical to NO and acetone.

Although an isotropic angular distribution was used for nearly all of the secondary dissociation pathways in this experiment, this particular channel merits further investigation. Since the primary C−Br bond fission does not impart significant rotational energy to the $CH_3C(NO_2)CH_3$ radical and the time scale of the secondary dissociation is most likely quite short, it is probable that this channel could have a specific angular distribution that is neither isotropic nor peaked at 0° and 180°. To investigate the angular distribution for this channel, the angle between the initial primary C−Br recoil vector and the secondary C−N recoil vector resulting from secondary C−N bond fission is calculated. To determine this angle, the initial C−Br bond fission recoil vector is mapped onto the transition state and the geometries from the intrinsic reaction coordinate (IRC) calculation; the angle is then calculated. This angle remains close to 70° throughout the dissociation (see discussion for further information). Since this

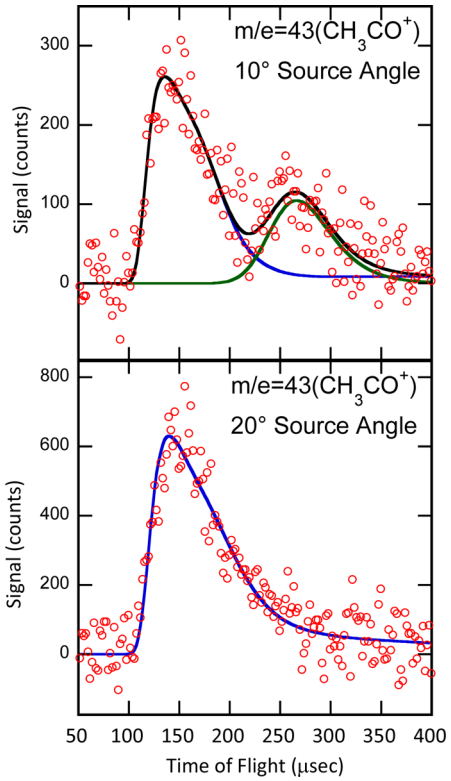

Figure 17. Time-of-flight spectrum taken at m/e = 43 of CH_3CO^+ at source angles of 10° and 20° (upper and lower frames, respectively). The data are shown as red circles. The signal arising from dissociative ionization of $CH_3C(O)CH_3$ fragments formed via secondary dissociation of vibrationally excited $CH_3C(NO_2)CH_3$ to NO + $CH_3C(O)CH_3$ (eq 7) is depicted as the blue line fit. The forward convolution blue fit was derived from the secondary angular distribution and $P(E_T, 2°)$ shown in Figures 18 and 19, respectively. The green fit (upper frame) shows the contribution from dissociative ionization of molecular clusters in the molecular beam.

angle is close to 90°, it is reasonable to assume that the angular distribution for this channel should resemble a sideways scattered distribution and therefore peak near 90° with lower amplitude at both 0° and 180°. The low amount of rotational energy imparted to the $CH_3C(NO_2)CH_3$ radicals would be expected to smear the angular distribution to a certain extent, however. The angular distribution used to fit this channel is shown in Figure 18 and is relatively broad with a peak at 90° and a drop off at both 0° and 180°.

The $P(E_T, 2°)$ for the secondary dissociation of NO + $(CH_3)_2CO$ is given in Figure 19. Forward convolution fitting using this $P(E_T, 2°)$ and the angular distribution in Figure 18 gives the blue line fit in the m/e = 43 TOF at two source angles (Figure 17). Further evidence for the dissociative ionization of acetone to CH_3CO^+ is given by the m/e = 43 $P(v)$ taken at 10.5 eV, above the appearance energy of CH_3CO^+ from acetone. This imaging speed distribution is broader than the m/e = 43 TOF and shown in the Supporting Information as Figure S5. Unlike the TOF data, the imaging data is affected by any additional velocity imparted to the product when a neutral species dissociatively ionizes, so when acetone dissociatively ionizes to CH_3CO^+ + CH_3, the image can show a broadened speed distribution. The cofragment NO is shown as the blue line fit in the m/e = 30 (NO^+) TOF and $P(v)$ (Figures 13 and 15, respectively). The blue line fit on the m/e = 30 TOF clearly completes the fast portion of the TOF spectrum.

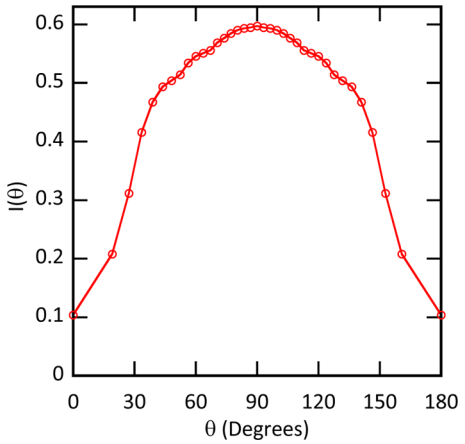

Figure 18. Angular distribution for the secondary dissociation of vibrationally excited $CH_3C(NO_2)CH_3$ to NO + $CH_3C(O)CH_3$ (eq 9).

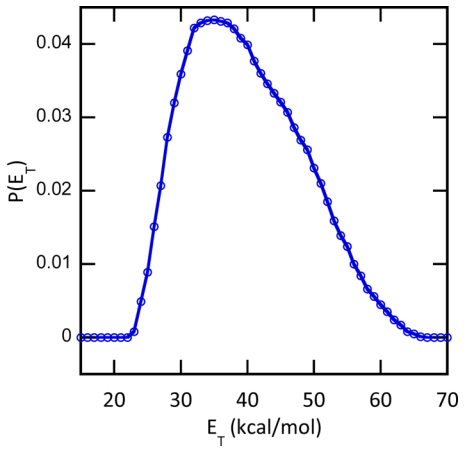

Figure 19. Product recoil kinetic energy distribution for the unimolecular dissociation of 2-nitro-2-propyl ($CH_3C(NO_2)CH_3$) radical to NO + $CH_3C(O)CH_3$ (eq 9). The combination of this $P(E_T, 2°)$ and the angular distribution in Figure 18 are used to generate the blue fits in Figures 13, 15, and 17.

E. Dissociation of the $CH_3C(NO_2)CH_3$ Radical to ($CH_3C(NO_2)$=CH_2) + H. Although the dissociation of vibrationally excited 2-nitro-2-propyl radical to 2-nitropropene + H

$$CH_3C(NO_2)CH_3 \rightarrow CH_3C(NO_2){=}CH_2 + H \qquad (10)$$

is the most endoergic product channel observed, its endoergicity of 42.5 kcal/mol is only 7 kcal/mol higher than the barrier for the dissociation to NO + acetone, and the C−H bond fission transition state is the looser of the two. Thus, signal from this channel is expected. Because of the large mass ratio between $CH_3C(NO_2){=}CH_2$ and H, the velocity of the resulting $CH_3C(NO_2){=}CH_2$ molecule is approximately the same as the velocity of the $CH_3C(NO_2)CH_3$ radical that underwent C−H fission. Therefore, the speed of the $CH_3C(NO_2){=}CH_2$ fragment in this secondary dissociation should be well predicted by only the primary $P(E_T)$ shown in Figure 7. Although no signal is recorded at m/e = 87 ($CH_3C(NO_2){=}CH_2^+$), it is reasonable to assume that m/e = 41 ($CH_3CCH_2^+$) is a major daughter crack of $CH_3C(NO_2){=}CH_2$. A forward convolution fit using the primary C−Br dissociation $P(E_T)$ yields the purple fit shown on the m/e = 41 TOF (Figure 12). This fit lines up with the sharp peak in the TOF providing further evidence for this channel.

F. Dissociation of the $CH_3C(NO_2)CH_3$ Radical to NO_2 + CH_2CHCH_3. The 2-nitro-2-propyl radical could in principle dissociate to NO_2 + propene

$$CH_3C(NO_2)CH_3 \rightarrow CH_3CH(NO_2){=}CH_2 \rightarrow NO_2 + CH_2CHCH_3 \quad (11)$$

via a 1,2 hydrogen shift followed by cleavage of the C−N bond (eq 11), but our data does not show evidence for this channel occurring. The signal at both m/e = 42 ($CH_2CHCH_3^+$) and m/e = 46 (NO_2^+) are well fit with contributions from other sources, and therefore, no signal at either mass is attributed to this channel. In addition, a RRKM calculation[27] predicts that this channel cannot compete with the other secondary dissociation channels following C−Br photofission as it has a higher barrier than the others and an entropically unfavorable transition state.

3. Dissociation of Vibrationally Excited $CH_3C(NO_2)CH_2$ Resulting from Primary HBr Elimination. *A. Overview.* The vibrationally excited $CH_3C(NO_2)CH_2$ molecules formed upon HBr elimination could potentially undergo five secondary dissociation processes. The energetics of each channel is shown in Figure 20. All endoergicities are relative to the zero-point corrected energy of 2-nitropropene. The pathway with the lowest barrier begins with the formation of a 4-membered ring with the oxygen bonded to both the nitrogen and the end $-CH_2$ carbon (50.0 kcal/mol). This isomer then undergoes concerted dissociation, over a barrier of 51.7 kcal/mol, cleaving both the N−O and C−C bonds to yield H_2CO + CH_3CNO. The second product channel is a concerted elimination of HONO, via two distinct five-center transition states, at 53.7 kcal/mol to give HONO + $CHCCH_3$ (propyne) and at 54.8 kcal/mol to give HONO + CH_2CCH_2 (allene). A third channel involves a nitro−nitrite isomerization over a barrier of 55.0 kcal/mol, followed by either the O−N bond breaking to form CH_3COCH_2 + NO (over a barrier of 21.0 kcal/mol) or a second isomerization where the NO group bonds to the end CH_2 carbon via a four-center transition state yielding $CH_3C(=O)CH_2(NO)$ with a barrier of 13.9 kcal/mol. Following the isomerization to $CH_3C(=O)CH_2(NO)$, either C−C or C−N bond fission may occur to yield $CH_3C{=}O$ + CH_2NO (20.0 kcal/mol) and CH_3COCH_2 + NO (14.2 kcal/mol), respectively. The most endoergic channel is fission of the C−N bond in $CH_3C(NO_2)CH_2$ with a bond dissociation energy of 67.9 kcal/mol and no barrier beyond the endoergicity. The data below give evidence for two of the five secondary dissociation pathways discussed here. These two pathways are designated by thicker lines and bolded text in Figure 20.

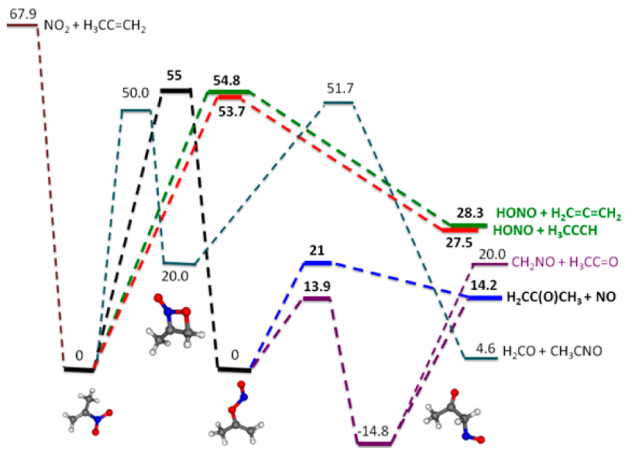

Figure 20. Calculated minima and transition states for the possible dissociation channels of the 2-nitropropene ($CH_3C(NO_2){=}CH_2$) on the ground state potential energy surface. All energies are expressed in units of kcal/mol and were calculated at the G4//B3LYP/6-311++g(3df,2p) level. The experimentally observed pathways are shown with thicker lines and bolded text.

B. Dissociation of $CH_3C(NO_2)CH_2$ to HONO + C_3H_4. Although there are two isomers of C_3H_4 that can form in this channel (propyne, $CHCCH_3$ and allene, CH_2CCH_2), the two pathways are assumed to have similar dynamics, so we fit them with the same $P(E_T, 2°)$, given in Figure S6, Supporting Information.

$$CH_3C(NO_2)CH_2 \rightarrow HONO + C_3H_4 \quad (12)$$

Forward convolution fitting using this $P(E_T, 2°)$, building on the velocities imparted to the 2-nitropropene photofragment, gives the dash−dot black line fit on the slow portion of the m/e = 40 ($C_3H_4^+$) net imaging speed distribution (Figure 21) derived from the data taken on our imaging apparatus. The high-speed portion of the data in Figure 21 is attributed to a secondary dissociation channel following primary HONO photoelimination (section 4.C). We only detect signal from the secondary HONO cofragment at daughter ions, not at the parent ion m/e = 47 ($HONO^+$). HONO dissociatively ionizes to m/e = 17 (OH^+) and m/e = 30 (NO^+); its contribution is shown in the dash−dot black line fit in the m/e = 30 (NO^+) TOF and the dashed black line fit m/e = 17 (OH^+) TOF (Figures 13 and 14, respectively).

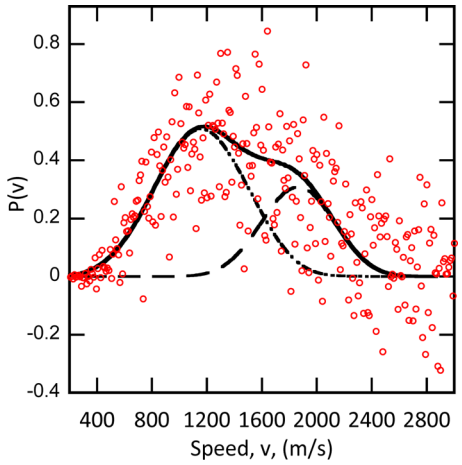

Figure 21. Speed distribution derived from the m/e = 40 ($C_3H_4^+$) image. Data are shown as red circles. The contribution of C_3H_4 products from the unimolecular dissociation of 2-nitropropene to HONO + C_3H_4 (eq 12) is shown in the dash−dot black fit. Forward convolution fitting of the signal from the dash−dot fit gives the $P(E_T, 2°)$ shown in Figure S6, Supporting Information. The dashed black line fit shows the contribution of C_3H_4 fragments from the dissociation of 2-bromopropene to C_3H_4 + HBr (eq 17). Forward convolution of the dashed black line fit gives the $P(E_T, 2°)$ shown in Figure S10, Supporting Information.

C. Dissociation of $CH_3C(NO_2)CH_2$ to CH_2NO + CH_3CO. Following isomerization to the $CH_3C(O)CH_2NO$ species, C−C bond fission can occur to give the products shown in eq 13.

$$CH_3C(NO_2)CH_2 \rightarrow CH_3C(ONO)CH_2 \rightarrow CH_3C(O)CH_2NO \rightarrow CH_2NO + CH_3CO \quad (13)$$

However, there is no experimental evidence of this channel occurring. Energetically, this channel is not expected to compete with the C−N bond fission reaction (Section 3.D) due to the higher barrier. There is no evidence of the CH_2NO species, and the m/e = 43 (CH_3CO^+) TOF is well fit with other sources (Section 2.D).

D. Dissociation of $CH_3C(NO_2)CH_2$ to CH_3CNO + CH_2O and NO + $CH_3C(O)CH_2$. Two product channels, giving fragments with identical masses, proceed through the following pathways: the first begins with the formation of a 4-membered ring with H_2CCNO framework, which is followed by C−C bond fission shown in eq 14 and the second involves isomerization of 2-nitropropene to 2-propenylnitrite, $CH_3C(ONO)CH_2$, which is followed by C−N bond fission (eq 15):

$$CH_3C(NO_2)CH_2 \rightarrow c\text{-}(H_2CON(O)C)CH_3 \rightarrow CH_3CNO + CH_2O \quad (14)$$

$$CH_3C(NO_2)CH_2 \rightarrow CH_3C(ONO)CH_2 \rightarrow CH_3C(O)CH_2NO \rightarrow NO + CH_3C(O)CH_2 \quad (15)$$

Both of these channels are energetically accessible and both produce fragments of the same masses. Since the fast portion of m/e = 30 (NO^+) $P(v)$ (Figure 15) is completely fit with other sources, both channels most likely would give signal in the slow portion of the m/e = 30 TOF. Because of dissociative ionization and other neutral NO species, it is extremely difficult to use this section of the m/e = 30 TOF to definitively assign channels. However, the lack of signal at m/e = 29 with 200 eV electron bombardment ionization demonstrates that formaldehyde is not present because CH_2O undergoes significant dissociative ionization to m/e = 29 (CHO^+). Therefore, the channel shown in eq 14 is assumed not to occur.

The $CH_3C(O)CH_2$ + NO channel, shown in eq 15, is expected to occur as it is the dissociation channel with the lowest barrier after the nitro−nitrite isomerization. However, using either the m/e = 30 (NO^+) TOF or $P(v)$ spectrum as evidence of this channel is difficult due to the multiple contributions appearing in both spectra. Additionally, no signal appears at m/e = 57 ($CH_3C(O)CH_2^+$) using either 10.5 or 200 eV ionization, but Alligood et al.[18,28] demonstrated that this species can either undergo dissociative ionization to give $CH_3CH_2^+$ (m/e = 29) or C−C bond fission to give CH_2CO + CH_3. Although signal does not appear at $CH_3CH_2^+$ (m/e = 29), it does at m/e = 42 (CH_2CO^+) and m/e = 15 (CH_3^+) at both 10.5 and 200 eV. Signal at m/e = 42 under 10.5 eV ionization has only a few possible sources. The slowest signal at m/e = 42 is assigned to the dissociative ionization of $CH_3C(Br)CH_3$ (Section 5.D) but this process is not expected to impart a significant amount of translational energy to the m/e = 42 ($CH_2CHCH_3^+$) fragment, and therefore, the majority of the faster m/e = 42 $P(v)$ signal (Figure 22) is assigned to the $CH_3C(O)CH_2$ + NO channel. There is also no evidence of CH_2CHCH_3 (mass 42) arising from the NO_2 + CH_2CHCH_3 secondary dissociation following primary C−Br fission (Section 2.F). Since there are seemingly no other channels likely to give relatively fast signal at m/e = 42, the unfit signal in the m/e = 42 $P(v)$, fit by the blue line, is given as evidence for this channel occurring (see next paragraph). In addition, while the m/e = 42 $P(v)$ is not bimodal and therefore difficult to be used diagnostically, the m/e = 15 (CH_3^+) TOF (Figure 23) is clearly bimodal with the slow peak arising most likely entirely from dissociative ionization of $CH_3C(Br)CH_3$. The high speed signal peaking near 150 μs evidence a contribution that we assign to methyl radicals from the dissociation of $CH_3C(O)$-

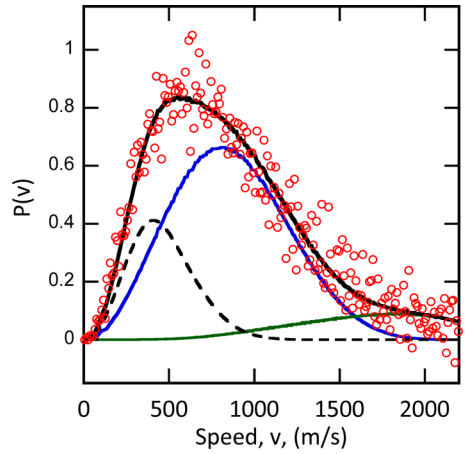

Figure 22. Speed distribution derived from the m/e = 42 ($C_3H_6^+$ and CH_2CO^+) image. Data are shown as red circles. The blue fit represents the contribution of CH_2CO fragments arising from the tertiary dissociation of vibrationally excited $CH_3C(O)CH_2$ fragments. This fit is created by use of $P(E_T, 3°)$ shown in Figure S8, Supporting Information. The slowest signal (dashed black fit) is assigned to the dissociative ionization of $CH_3C(Br)CH_3$ fragments from primary C−NO_2 photofission. Forward convolution of this fit gives the $P(E_T, 2°)$ shown in Figure S12, Supporting Information. The green fit is tentatively assigned to dissociative ionization of $CH_3C(O)CH_3$ fragments from secondary dissociation of $CH_3C(NO_2)CH_3$ radicals to $CH_3C(O)CH_3$ + NO (eq 15).

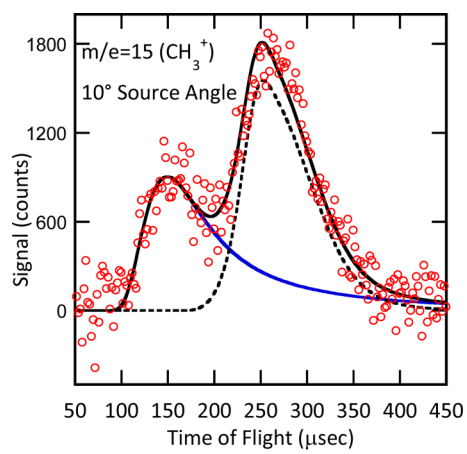

Figure 23. Time-of-flight spectrum taken at m/e = 15, CH_3^+. Data are shown as red circles. The blue fit is the contribution of methyl radicals formed from the tertiary dissociation of vibrationally excited $CH_3C(O)CH_2$ fragments. Forward convolution fitting of the signal in the blue fit gives the $P(E_T, 3°)$ shown in Figure S8, Supporting Information. Dissociative ionization of $CH_3C(Br)CH_3$ fragments resulting from primary C−NO_2 photofission is shown by the short dashed black fit.

CH_2 originating from the $CH_3C(O)CH_2$ + NO channel (eq 15).

Although the evidence for this channel is clear, the $P(E_T, 2°)$ is hard to acquire directly from either the $CH_3C(O)CH_2$ (no signal) or NO (other sources) fragments that originate from the secondary dissociation event. Therefore, joint optimization of the $P(E_T, 2°)$ and $P(E_T, 3°)$ for this channel is done using the m/e = 42 $P(v)$ and m/e = 15 TOF. This type of optimization is possible because of the large mass difference between the two fragments CH_2CO (mass 42) and CH_3 (mass 15). Because of this difference, the CH_3 fragment will carry away a much larger fraction of the relative velocity imparted during the tertiary dissociation and thus be more sensitive to the $P(E_T, 3°)$, whereas the m/e = 42 will be more sensitive to the $P(E_T, 2°)$ since it carries away a small fraction of the tertiary relative velocity imparted during the $CH_3C(O)CH_2$ dissociation. Joint optimization yields the $P(E_T, 2°)$ and $P(E_T, 3°)$ shown in Figures S7 and S8, Supporting Information, respectively. Forward convolution using the $P(E_T, 2°)$ in Figure S7, Supporting Information, gives the double dash−dot black line fit in the m/e = 30 (NO^+) TOF and $P(v)$ (Figures 13 and 15). Forward convolution using the $P(E_T, 3°)$ in Figure S8, Supporting Information, gives the blue line fit in the m/e = 42 (CH_2CO^+) $P(v)$ and the m/e = 15 (CH_3^+)TOF.

E. Dissociation of $CH_3C(NO_2)CH_2$ to NO_2 + CH_2CCH_3. The experimental data do not show evidence for this channel occurring. The signal at both m/e = 41 (CH_2CCH_3) and m/e = 46 (NO_2) are well fit with contributions from other sources, and therefore, no signal at either mass is attributed to this channel. In addition, the barrier to this channel is much higher than any alternative secondary dissociation channels after HBr elimination, so it is not expected to compete.

4. Dissociation of Vibrationally Excited HONO and $CH_3C(Br)CH_2$ Resulting from Primary HONO Photoelimination. *A. Overview.* The low endoergicity of primary HONO elimination (+15.7 kcal/mol) yields in excess of 130 kcal/mol of remaining energy when 2-bromo-2-nitropropane is photodissociated at 193 nm. The $P(E_T)$ for this primary channel in Figure 5 shows that the recoil kinetic energies partitioned into the photofragments are small (<20 kcal/mol) leaving over 100 kcal/mol of internal energy to be distributed among the two fragments HONO and $CH_3C(Br)CH_2$. Thus both of these photoproducts may undergo secondary dissociation. The HO−NO bond dissociation energy, HONO → NO + OH, is calculated as 49.9 kcal/mol, well below the available internal energy. The cofragment $CH_3C(Br)CH_2$ can lose a Br atom or undergo concerted elimination of HBr. The C−Br bond energy was calculated as 77.6 kcal/mol, and the barrier to HBr elimination was calculated at 64.8 kcal/mol, so one might expect that the HBr loss channel will dominate due to the lower barrier. The experimental results follow.

B. Dissociation of HONO to Yield NO and OH. The internal energy of the HONO product from primary HONO photoelimination is expected to be sufficient (see above) for dissociating into OH + NO.

$$\text{HONO} \rightarrow \text{OH} + \text{NO} \tag{16}$$

Nevertheless, it is difficult to distinguish between dissociative ionization and neutral fragment dissociation for this channel because both HONO and OH have ionization energies that are above 10.5 eV and so cannot be detected in our imaging apparatus. Saha and co-workers[9] detected OH LIF signal from the photodissociation of 2-bromo-2-nitropropane, however, so we took a TOF spectrum at m/e = 17 using 200 eV electron bombardment to detect any fragments appearing as OH^+. The m/e = 17 (OH^+) TOF, given in Figure 14, provides the first piece of evidence for the occurrence of this channel. The only other secondary dissociation channel, which could give OH as a neutral fragment, is OH + $CH_3C(NO)CH_2$ from primary C−Br fission and is presumed to not occur (see Section 2.B). The two secondary HONO elimination channels, eqs 8 and 12, give HONO that can dissociatively ionize to OH^+ upon 200 eV electron bombardment, but neither give HONO with high enough net speeds to fit the fast edge of the m/e = 17 TOF in Figure 14. Thus, the only process that could produce OH product with high enough velocities to fit the fast edge of this spectrum is the dissociation of vibrationally excited HONO to OH + NO (all neutral species). The $P(E_T, 2°)$ for this dissociation of HONO to OH + NO is depicted in Figure S9, Supporting Information. This $P(E_T, 2°)$ peaks near 2 kcal/mol, which is physically reasonable for a simple bond fission reaction. Building on the initial HONO velocities in this two-step mechanism gives the orange fit in the m/e = 17 (OH^+) TOF (Figure 14). (The net imaging speed distribution of the OH product, peaking near 1200 m/s, is, however, much slower than that deduced from the Doppler measurements of Saha and co-workers.) The NO coproduct formed in this secondary channel is given by the orange line fit in the m/e = 30 (NO^+) TOF and net imaging speed distribution (Figures 13 and 15, respectively). This channel fits very well on the slow peak in the m/e = 30 imaging speed distribution giving further support for its occurrence.

C. Dissociation of $CH_3C(Br)CH_2$ to Yield HBr and C_3H_4. The $CH_3C(Br)CH_2$ cofragment formed upon primary HONO photoelimination can also have enough internal energy to undergo secondary dissociation. One possible channel is

$$CH_3C(Br)CH_2 \rightarrow HBr + C_3H_4 \tag{17}$$

A signal at m/e = 40 ($C_3H_4^+$) evidences a contribution from this channel. Although there is another secondary channel that can give C_3H_4 (one following HBr primary photoelimination), it is difficult to devise a single $P(E_T, 2°)$ that fits the m/e = 40 ($C_3H_4^+$) imaging speed distribution given in Figure 21. Thus, we fit this data with both processes. Using the secondary $P(E_T, 2°)$ shown in Figure S10, Supporting Information, we can fit the contribution to our data from both momentum matched fragments of the reaction in eq 17, the C_3H_4 at m/e = 40 ($C_3H_4^+$) and the HBr at m/e = 80 ($H^{79}Br^+$). Forward convolution fitting using this $P(E_T, 2°)$ gives the dashed black line in the m/e = 40 ($C_3H_4^+$) imaging speed distribution (Figure 21) and the green fit in the m/e = 80 ($H^{79}Br^+$) TOF (Figure 9). This channel fits well on the fast edge of the m/e = 80 TOF and is confirmed by the appearance of both momentum matched fragments. We did not attempt to selectively ionize CH_2CCH_2 or $CHCCH_3$, so we assume that the translational energy distributions for the dissociation to HBr + CH_2CCH_2 or $CHCCH_3$ would not be significantly different as they both involve 4-center transition states and similar endoergicities.

5. Dissociation of Vibrationally Excited $CH_3C(Br)CH_3$ Resulting from Primary C−NO_2 Photofission. *A. Overview.* The vibrationally excited $CH_3C(Br)CH_3$ radicals resulting from C−NO_2 photofission can undergo several secondary dissociation channels. The lowest barrier is associated with loss of a hydrogen atom to give $CH_3C(Br)CH_2$ + H with a barrier of 37.9 kcal/mol. The next two dissociation channels occur after a

1,2-hydrogen shift, which gives $CH_2CH(Br)CH_3$. The optimized geometry for this species shows an abnormally long C−Br bond and resembles a loosely bound complex between Br and CH_2CHCH_3. Following this hydrogen shift, the molecule has two possible dissociation pathways. The first is C−Br bond fission with a barrier of 10.4 kcal/mol. The second channel yields HBr + CH_2CHCH_2 via a hydrogen abstraction reaction with a barrier of 14.5 kcal/mol. The calculated pathway for HBr elimination has a transition state to a loosely bonded complex between the CH_3 group and the bromine atom. This complex can then undergo an intramolecular hydrogen abstraction channel to yield HBr. As mentioned in Section 1.B, the NO_2 fragments that possess low amounts of translational energy are extremely likely to absorb a second 193 nm photon and dissociate to NO + O.

B. Photodissociation of NO_2 to Yield NO + O. The NO_2 fragments with high internal energy are capable of absorbing a second 193 nm photon and dissociating to NO + O, detailed in eq 18.

$$NO_2 + h\nu \rightarrow NO + O \tag{18}$$

This phenomenon was demonstrated by Butler et al. in their study of the photodissociation of nitromethane at 193 nm.[21] Using the $P(E_T, h\nu, 2°)$ (reproduced in Figure S11, Supporting Information), determined in the appendix of ref 21, we vector-add those velocities (with an isotropic secondary $I(\theta)$) to the velocities of the NO_2 lost to this process (see Section 1.B) to predict the signal onsets in our m/e = 30 (NO^+) TOF and imaging data. This signal is shown as the fine black dotted line fit in the m/e = 30 TOF and $P(v)$ (Figures 13 and 15, respectively).

C. Dissociation of $CH_3C(Br)CH_3$ to Yield $CH_3C(Br)CH_2$ + H. Though we expect the vibrationally excited $CH_3C(Br)CH_3$ cofragment formed in primary C−NO_2 photofission to be able to dissociate as follows:

$$CH_3C(Br)CH_3 \rightarrow CH_3C(Br)CH_2 + H \tag{19}$$

the predicted speed distribution of the heavy $CH_3C(Br)CH_2$ product would have a nearly identical velocity distribution to the dissociating 2-bromo-2-propyl radical. Predicting the speed distribution using the primary C−NO_2 photofission $P(E_T)$ in Figure 2 gives the imaging speed distribution shown in black open circles in Figure 4 at m/e = 122, so would be strongly overlapped by the signal we detected from the primary HONO photoelimination cofragment. Thus, we were unable to characterize this product channel.

D. Dissociative Ionization of $CH_3C(Br)CH_3$ to Yield $CH_3CHCH_2^+$ + Br. Evidence for this process is given in the appearance of a very slow signal at m/e = 42 with 10.5 eV ionization. This signal is too slow to have originated from the $CH_3C(NO_2)CH_3$ radical (Section 2) or the tertiary dissociation of $CH_3C(O)CH_2$ (Section 3.D) and is therefore attributed to the dissociative ionization of $CH_3C(Br)CH_3$ (eq 20) with a calculated appearance energy of 10.18 eV.

$$\begin{aligned} CH_3C(Br)CH_3^+ &\rightarrow CH_2CH(Br)CH_3^+ \\ &\rightarrow CH_3CHCH_2^+ + Br \end{aligned} \tag{20}$$

Although this mass could arise from neutral dissociation of the $CH_3C(Br)CH_3$ radical, the neutral dissociation can only occur after a 1,2-hydrogen shift and is not expected to compete with the lower energy H-loss channel (Section 5.C). These radicals likely have significant vibrational energy (although below the barrier for the 1,2-hydrogen shift), which further corroborates this assignment. The $P(E_T, 2°)$ for this dissociative ionization (occurring on the cationic surface) is given in Figure S12, Supporting Information. Forward convolution fitting using this $P(E_T, 2°)$ gives the dashed black line fit in the m/e = 42 ($CH_3CHCH_2^+$) $P(v)$ (Figure 22).

E. Dissociative Ionization of $CH_3C(Br)CH_3$ to Yield $CH_3CCH_2^+$ + HBr. Evidence for this process is given as the appearance of slow signal in the m/e = 41 ($C_3H_5^+$) $P(v)$ (Figure 11). Most of the signal in this $P(v)$ is assigned to the secondary HONO elimination channel from primary C−Br photofission (see Section 2.C) but this channel is incapable of giving CH_3CCH_2 fragments with low enough translational energies to fit on the slow edge of the m/e = 41 imaging speed distribution. Although this signal could be from the analogous neutral dissociation, this would not be expected to compete with the H-loss channel (eq 19) due to the larger barrier height and tighter transition state. Therefore, this signal is attributed the dissociative ionization process detailed in eq 21 with a calculated appearance energy of 9.2 eV.

$$CH_3C(Br)CH_3^+ \rightarrow CH_3CCH_2^+ + HBr \tag{21}$$

The $P(E_T, 2°)$ for this process is shown in Figure S13, Supporting Information. The corresponding fit is shown as the dashed black line in the m/e = 41 $P(v)$ (Figure 11).

■ DISCUSSION

In this study, we demonstrate that 2-bromo-2-nitropropane has four primary photodissociation channels at 193 nm and characterize the subsequent dissociation events of species produced in the primary channels. The five observed secondary dissociation pathways for the two fragments of interest, 2-nitro-2-propyl radical and 2-nitropropene, are shown in bold text and thicker pathway lines in Figures 10 and 20, respectively. Both of these fragments undergo HONO and NO loss channels. These channels are useful mimics for elucidating the thermal decomposition mechanisms of larger energetic materials with geminal dinitro groups, such as TNAZ and FOX-7.

Calculations performed by Alavi et al.[7] show that subsequent to initial C−NO_2 cleavage in TNAZ, the resulting radical will undergo a ring-opening reaction yielding the $CH_2{=}C(NO_2)$-$CH_2N(NO_2)$ fragment with unpaired electron density on the nitramine nitrogen atom. The 2-nitropropene molecule formed after primary HBr elimination (Section 1.E) in our experiment mimics the nitroalkene section of TNAZ after ring-opening. Our results with $CH_2{=}C(NO_2)CH_3$ show that secondary loss of NO_2 from the carbon atom does not occur but that the molecule rather produces either HONO, in a concerted fashion, or undergoes a nitro−nitrite isomerization yielding NO. Interestingly, these results suggest that TNAZ may not undergo secondary NO_2 loss (as suggested in ref 8) from the carbon atom following ring-opening either, which supports the results presented by Zhang and Bauer[1] and the computational study of Alavi et al.[7] However, while a direct comparison between these two molecules is not possible due to the fact that the $CH_2{=}C(NO_2)CH_3$ molecule in our study does not include the nitrogen radical center, some inferences may be made. For instance, the nitrogen radical center would most likely be delocalized into the N−NO_2 group and not directly influence the electron density in the C−NO_2 bond. Therefore, it is probable that the presence of the radical would not greatly enhance secondary NO_2 production from the remaining C−

NO_2 group. In fact, Alavi et al.[7] calculates secondary loss of NO_2 (from the alkyl group) to be the highest channel energetically following ring-opening. This same reasoning may be used to conclude that the nitrogen radical does not significantly affect the extent of the nitro−nitrite isomerization at the C−NO_2 group and subsequent production of NO. The HONO production in our results may, however, be directly influenced by the presence of the radical in TNAZ. In the case of $CH_2{=}C(NO_2)CH_3$, there is little difference energetically between which C−H bond is broken to create the HONO fragment. In TNAZ, it is reasonable to assume that the radical on the nitrogen would interact with the antibonding σ orbital of the adjacent C−H bond (similar to hyperconjugation, but at the barrier to C−H bond fission when the σ^* orbital is lower in energy). This would reduce the barrier to C−H bond fission and make it more likely to be broken during the elimination of HONO. It is difficult to conclude whether this preference would increase or decrease the extent of HONO elimination, however.

The 2-nitro-2-propyl radical formed after primary C-Br photofission (Section 1.D) in our experiment mimics the nitroalkyl radical of TNAZ after initial C−N bond fission. Comparisons are difficult, however, since the radical formed in our study, $CH_3C(NO_2)CH_3$, does not include the strained ring found in TNAZ, but some generalizations can still be made. The lowest pathway to secondary NO_2 production in the $CH_3C(NO_2)CH_3$ radical involves a 1,2-hydrogen shift, which precedes the C−N bond fission. The presence of the strained ring would make this 1,2-hydrogen shift even less likely due to the strained geometry of the ring. Furthermore, loss of NO_2 would then create a strained unsaturated four-membered ring, which is even more unstable. Therefore, the lack of observed secondary NO_2 signal in our experiments is in accord with the conclusion that TNAZ will undergo a ring-opening reaction rather than lose a second NO_2 group.

One of the common functionalities in energetic materials is the nitroalkyl (or geminal dinitroalkyl) moiety. Consequently, NO is usually produced following a nitro−nitrite isomerization during the decomposition of energetic materials. The nitrite isomer is usually a stable structure (a local minimum in the PES) in energetic materials. However, as the first step in the decomposition mechanism is loss of NO_2, it is the species where one NO_2 group remains that undergoes the subsequent dissociation steps. Our calculations done in this study have shown that the introduction of a radical at the carbon atom of the C−NO_2 center has the potential to significantly change the mechanism of this isomerization. Specifically, calculations on the unimolecular decomposition of the 2-nitro-2-propyl ($CH_3C(NO_2)CH_3$) radical established two different pathways to the production of neutral NO products. The higher energy path (P1), with a ZPE corrected barrier of 62.5 kcal/mol, is similar to the traditional nitro−nitrite isomerization, whereas the lower energy path (P2), with a ZPE corrected barrier of 35.7 kcal/mol, goes through a completely different intermediate where the carbon, nitrogen, and one oxygen form a three-membered ring. The optimized transition state geometries for both paths are shown in Figure 24 where TS1 goes with P1. Whereas TS1 has equal and long C−N and C−O bond lengths of 1.94 Å (similar to a traditional nitro−nitrite isomerization), TS2 maintains a strong C−N bond (R_{C-N} = 1.37 Å), while the O atom is developing a bond to the carbon (R_{C-O} = 1.9 Å). The C−N bond in TS2 is actually slightly shorter than in the starting radical (1.42 Å), whereas the C−N bond in TS1 is

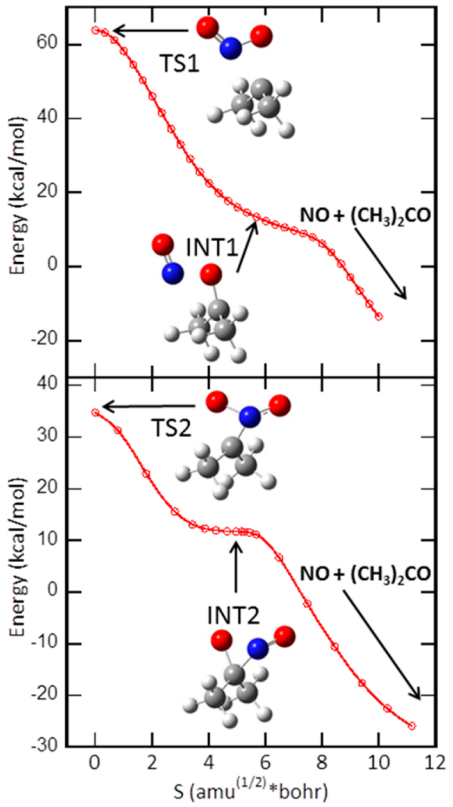

Figure 24. Intrinsic reaction coordinate (IRC) calculations performed at the B3LYP/6-311++g(3df,2p) level. Upper frame: IRC of NO loss via a nitrite intermediate (INT1) from 2-nitro-2-propyl radical (P1). Lower frame: IRC of NO loss via a saturated carbon center (INT2) from 2-nitro-2-propyl radical (P2). Energy is reported relative to the energy of the $CH_3C(NO_2)CH_3$ radical calculated at the B3LYP/6-311++g(3df,2p) level and is not corrected for zero-point energy. Geometries of the transition states (TS) and intermediates (INT) for both pathways (P1 and P2) of NO production from the 2-nitro-2-propyl radical are shown on their respective IRC plot. All geometry optimizations were performed at the B3LYP/6-311++g(3df,2p) level. Adapted from ref 29. Copyright 2012 American Chemical Society.

quite close to homolytic cleavage. In fact, the energy of TS1 is within 15 kcal/mol of the calculated C−N bond fission asymptote (75 kcal/mol). This is likely the reason for the large energy difference between these two transition states.

On the surface it would appear that either TS1 or TS2 could pass through a nitrite isomer intermediate, but the IRC calculations show that this is not the case. The IRC pathways for both paths are shown in Figure 24 where the upper and lower frames represent P1 and P2, respectively. Interestingly both pathways show the same shoulder character on the IRC, where the slope becomes very flat and resembles convergence to a local minimum geometry. In fact, the structures on the shoulders are not true minima but rather intermediate structures on the path to NO loss. These intermediates are shown in Figure 24 with their respective TS and labeled as INT1 and INT2. The geometry of INT1 is very similar to a nitrite isomer with C−O−NO bonding. However, the nitrite isomer is not a local minimum because of the radical on the center carbon. The energy along the reaction coordinate drops steeply as the double bond forms between the C and the O atoms en route to NO + acetone. In contrast, the geometry of INT2 resembles a carbon center with four bonds where the center carbon is part of a three-membered ring with the N and

O atoms. As INT2 evolves toward products, there is a repulsive force between the C and N atoms as the double bond is formed between the C and O atoms. The shoulders on the IRC are a consequence of the energetic balance between bond breaking and bond forming. The lower energy pathway (P2) to NO loss does not exist with the closed shell 2-nitropropene species, however. For that molecule, the nitrite isomer is a local minimum and there was only one TS found for the isomerization.

This phenomenon may be relevant to energetic materials that possess a nitroalkyl radical center on the path to decomposition by giving a lower energy path to NO production. An example of this is 1,1-diamino,2,2-dinitroethene (FOX-7) where the two NO_2 groups are on the same carbon (it is unclear whether the alkene character would affect this pathway). In the case of TNAZ, however, the presence of the strained ring ensures that the ring-opening reaction will dominate over any reactions on the radical center. For example, although FOX-7 has a double bond rather than a single to the adjacent carbon, this lower energy path may exist for it or for similar materials following initial loss of NO_2. This pathway to NO production is extremely exothermic and the availability of this lower energy barrier may be responsible for the quick release of energy observed in energetic materials with geminal dinitro functional groups.

Although all of the data presented in this study is well fit with the theory presented in this article, the lack of definitive signal from the OH + $CH_3C(NO)CH_2$ channel is interesting. Energetically, this channel has the lowest barrier on the potential energy surface for 2-nitro-2-propyl radical, although the formation of a hydrogen bonded complex en route may significantly decrease the extent of this pathway relative to the simple C−N bond fission to produce HONO. Although this channel was not used in fitting our data, possible evidence for its occurrence is given by the apparent ionization energy dependence shown by the fast edge of the m/e = 41 image (Figure 11, lower frame). The slight suppression of the fast signal at lower IE (8.87 eV) suggests that there is a fast fragment at m/e = 41 arising from dissociative ionization. In the Supporting Information, we show a possible $P(E_T)$ for this signal (Figure S1); forward convolution fitting using this $P(E_T)$ predicts that the net speed of the OH fragments peaks at ∼3000 m/s, matching the Doppler measurements of Saha et al.[9] Therefore, despite the lack of signal at m/e = 71 ($CH_3C(NO)CH_2^+$) at any IE used in this study, there is possible evidence that this channel occurs to a small extent. While this channel may occur, most of the neutral OH products fit in this study possess much lower speeds than observed by Saha et al.[9] This discrepancy remains unresolved.

In section 2.D, the secondary dissociation of 2-nitro-2-propyl radical to NO + $CH_3C(O)CH_3$ was fit using an anisotropic angular distribution, which resembles a sideways scattering event. Qualitatively, what determines the angular dependence, in this case, is the angle between the initial C−Br bond fission recoil vector and the repulsive vector along the C−N bond axis in the dissociation event to NO + $CH_3C(O)CH_3$. These two vectors are shown in the Supporting Information as Figure S14 on the geometry of INT2 right before dissociation taken from the IRC of the $CH_3C(NO_2)CH_3$ radical to NO + $CH_3C(O)$-CH_3; this angle remains close to 70° throughout the dissociation. Since the time scale of the dissociation is most likely quite small, it is reasonable to assume that sideways scattering events would dominate the dissociation to NO + $CH_3C(O)CH_3$ and therefore motivates the decision to fit this channel using the sideways angular distribution shown in Figure 18. The angular distribution that fit the data is quite broad, but peaked in the sideways direction. Note that there is not much rotational energy imparted to the 2-nitro-2-propyl radical from the C−Br fission. Although the angular distribution in Figure 18 is physically reasonable, it should be noted that the distribution was derived empirically from the m/e = 43 (CH_3CO^+) and m/e = 30 (NO^+) TOFs and therefore has significant uncertainty associated with it.

■ CONCLUSIONS

This study first investigated the photodissociation of 2-bromo-2-nitropropane, characterizing four primary photodissociation channels at 193 nm. It then characterized the subsequent dissociation events of species produced in the primary channels, most importantly the 2-nitro-2-propyl radical and 2-nitro-propene. The latter allows one to assess the relative importance of some of the subsequent decomposition channels proposed in the thermal decomposition of TNAZ, after initial C−NO_2 fission. While early work[8] concluded that the molecule lost a second NO_2 group, our experimental results concur with the later computational results of Alavi et al.[7] that showed that loss of a second NO_2 group after ring-opening would not compete effectively with the other available decomposition channels. Our results on 2-nitro-2-propyl radical reveal an important mechanism in the decomposition channels of energetic materials with geminal dinitro groups but no strained ring (e.g., FOX-7). We show that NO loss from 2-nitro-2-propyl radical occurs not by the traditional nitro−nitrite isomerization pathway, but rather via a 3-membered ring pathway with a 26.8 kcal/mol lower barrier. This provides a low barrier decay path to the highly exothermic product channel of NO + acetone.

■ ASSOCIATED CONTENT

Supporting Information

An alternate fit to the data presented in Section 2.B is shown in Figures S1−S3. The m/e = 43 imaging speed distribution is shown in Figure S5. Product recoil kinetic energy distributions for the dissociations shown in eq 8 (Figure S4), eq 12 (Figure S6), eq 15 (Figures S7 and S8), eq 16 (Figure S9), eq 17 (Figure S10), eq 18 (Figure S11), eq 20 (Figure S12), and eq 21 (Figure S13). A detailed diagram showing the recoil vectors involved in the loss of NO from vibrationally excited $CH_3C(NO_2)CH_3$ radical is given in Figure S14 (see Section 2.D). The raw m/e = 43 (CH_3CO^+) image is shown in Figure S15. The raw images for each speed distribution presented in the text are presented in Figures S16−S22. This material is available free of charge via the Internet at http://pubs.acs.org.

■ AUTHOR INFORMATION

Corresponding Author

*(L.J.B.) E-mail: l-butler@uchicago.edu. Phone: 773-702-7206.

Notes

The authors declare no competing financial interest.

■ ACKNOWLEDGMENTS

This material is based upon work supported by the U.S. Army Research Laboratory and the U.S. Army Research Office under contract number W911NF-10-1-0314. Some of the equipment used in this experiment was supported by DURIP-ARO under grant number W911NF-10-1-1049. We gratefully acknowledge

Robert Radway for his help in the scattering lab and the supplemental HSAP funding provided by U.S. Army Research Office. We also gratefully acknowledge C. C. Womack for her help in making the program to analyze the angles between primary and secondary recoil vectors as well as help in taking imaging lab data.

■ REFERENCES

(1) Zhang, Y.-X.; Bauer, S. H. Gas-Phase Decomposition Mechanisms of C-NO_2, N-NO_2 Energetic Materials: Reevaluations. *Int. J. Chem. Kinet.* **1999**, *31*, 655−673.

(2) Guo, Y. Q.; Greenfield, M.; Bhattacharya, A.; Bernstein, E. R. On the Excited Electronic State Dissociation of Nitramine Energetic Materials and Model Systems. *J. Chem. Phys.* **2007**, *127*, 154301.

(3) Guo, Y. Q.; Bhattacharya, A.; Bernstein, E. R. Excited Electronic State Decomposition of Furazan Based Energetic Materials: 3,3-Diamino-4,4-Azoxyfurazan and its Model Systems, Diaminofurazan and Furazan. *J. Chem. Phys.* **2008**, *128*, 034303.

(4) Bhattacharya, A.; Guo, Y. Q.; Bernstein, E. R. Unimolecular Decomposition of Tetrazine-*N*-Oxide Based High Nitrogen Content Energetic Materials from Excited Electronic States. *J. Chem. Phys.* **2009**, *131*, 194304.

(5) Yu, Z.; Bernstein, E. R. Decomposition of Pentaerythritol Tetranitrate [$C(CH_2ONO_2)_4$] Following Electronic Excitation. *J. Chem. Phys.* **2011**, *135*, 154305.

(6) Garland, N. L.; Nelson, H. H. Laser-Induced Decomposition of TNAZ. *J. Phys. Chem. B* **1998**, *102*, 2663−2667.

(7) Alavi, S.; Reilly, L. M.; Thompson, D. L. Theoretical Predictions of the Decomposition Mechanism of 1,3,3-Trinitroazetidine (TNAZ). *J. Chem. Phys.* **2003**, *119*, 8297−8304.

(8) Anex, D. S.; Allman, J. C.; Lee, Y. T. Studies of Initial Dissociation Processes in 1,3,3-Trinitroazetidine by Photofragmentation Translational Spectroscopy. In *Chemistry of Energetic Materials*; Olah, G. A., Squire, D. R., Eds.; Academic Press: New York, 1991; pp 27−54.

(9) Saha, A.; Kawade, M.; Upadhyaya, H. P.; Kumar, A.; Naik, P. D. Laser-Induced UV Photodissociation of 2-Bromo-2-nitropropane: Dynamics of OH and Br Formation. *J. Chem. Phys.* **2011**, *134*, 044316.

(10) Lee, Y. T.; McDonald, J. D.; Lebreton, P. R.; Herschbach, D. R. Molecular Beam Reactive Scattering Apparatus with Electron Bombardment Detector. *Rev. Sci. Instrum.* **1969**, *40*, 1402−1408.

(11) Daly, N. R. Scintillation Type Mass Spectrometer Ion Detector. *Rev. Sci. Instrum.* **1960**, *31*, 264−267.

(12) CMLAB2, version 6/93, modified by J. D. Myers. This is an interactive version built on the original cmlab2 program: X. Zhao, Ph.D. dissertation, University of California, 1988.

(13) Eppink, A. T. J. B.; Parker, D. H. Velocity Map Imaging of Ions and Electrons Using Electrostatic Lenses: Application in Photoelectron and Photofragment Ion Imaging of Molecular Oxygen. *Rev. Sci. Instrum.* **1997**, *68*, 3477−3484.

(14) Chang, B.; Hoetzlein, R. C.; Mueller, J. A.; Geiser, J. D.; Houston, P. L. Improved Two-Dimensional Product Imaging: The Real-Time Ion-Counting Method. *Rev. Sci. Instrum.* **1998**, *69*, 1665−1670.

(15) Chandler, D. W.; Houston, P. L. Two-Dimensional Imaging of State-Selected Photodissociation Products Detected by Multiphoton Ionization. *J. Chem. Phys.* **1987**, *87*, 1445−1447.

(16) Ratliff, B. J.; Tang, X.; Butler, L. J.; Szpunar, D. E.; Lau, K. Determining the $CH_3SO_2 \rightarrow CH_3 + SO_2$ Barrier from Methylsulfonyl Chloride Photodissociation at 193 nm Using Velocity Map Imaging. *J. Chem. Phys.* **2009**, *131*, 044304.

(17) Dribinski, A.; Ossadtchi, V. A.; Mandelshtam; Reisler, H. Reconstruction of Abel-Transformable Images: The Gaussian Basis-Set Expansion Abel Transform Method. *Rev. Sci. Instrum.* **2002**, *73*, 2634.

(18) Alligood, B. W.; FitzPatrick, B. L.; Szpunar, D. E.; Butler, L. J. Chloroacetone Photodissociation at 193 nm and the Subsequent Dynamics of the $CH_3C(O)CH_2$ Radical: An Intermediate Formed in the OH + Allene Reaction En Route to CH_3 + Ketene. *J. Chem. Phys.* **2011**, *134*, 054301.

(19) Curtiss, L. A.; Redfern, P. C.; Raghavachari, K. Gaussian-4 Theory. *J. Chem. Phys.* **2007**, *126*, 084108.

(20) Frisch, M. J.; Trucks, G. W.; Schlegel, H. B.; et al. *Gaussian 09*, revision A.02; Gaussian, Inc.: Wallingford, CT, 2009.

(21) Butler, L. J.; Krajnovich, D.; Lee, Y. T. The Photodissociation of Nitromethane at 193 nm. *J. Chem. Phys.* **1983**, *79*, 1708−1722.

(22) Vinodkumar, M.; Dave, R.; Bhutadia, H.; Antony, B. K. Electron Impact Total Ionization Cross Sections for Halogens and Their Hydrides. *Int. J. Mass. Spectrom.* **2010**, *292*, 7−13.

(23) NIST Mass Spectrometry Data Center. http://webbook.nist.gov.

(24) Hayes, T. R.; Wetzel, R. C.; Freund, R. S. Absolute Electron-Impact-Ionization Cross-Section Measurements of the Halogen Atoms. *Phys. Rev. A* **1987**, *35*, 578−584.

(25) Sakaizumi, T.; Imajo, H.; Yamasaki, R.; Usami, T.; Kawaji, S.; Abe, S.; Haraga, T.; Morii, H.; Kuze, N.; Ohashi, O. Generation, Microwave Spectrum, Barrier to Internal Rotation of Methyl Group, and ab Initio MO Calculation of *syn*-2-Nitrosopropene, *syn*-$CH_2{=}C(CH_3){-}N{=}O$. *J. Mol. Spectrosc.* **2000**, *204*, 26−35.

(26) Krisch, M. J.; Reid, M. C.; McCunn, L. R.; Butler, L. J.; Shu, J. Photofragment Translational Spectroscopy of Nitric Acid at 248 nm with VUV Photoionization Detection of Products. *Chem. Phys. Lett.* **2004**, *397*, 21−25.

(27) The RRKM code is obtained from W. L. Hase and D. L. Bunker, *Quantum Chemistry Program Exchange* 234, (1974). To calculate the sums and densities of states, we used the Whitten Rabinovitch semiclassical technique implemented in that software.

(28) Alligood, B. W.; Womack, C. C.; Brynteson, M. D.; Butler, L. J. Dissociative Photoionization of $CH_3C(O)CH_2$ to $C_2H_5^+$. *Int. J. Mass. Spectrom.* **2011**, *304*, 45−50.

(29) Booth, R. S.; Lam, C.-S.; Butler, L. J. A Novel Mechanism for Nitric Oxide Production in Nitroalkyl Radicals that Circumvents Nitro−Nitrite Isomerization. *J. Phys. Chem. Lett.* **2013**, *4*, 547−550.